

Changes in stratospheric aerosol extinction coefficient after the 2018 Ambae eruption as seen by OMPS-LP and ~~ECHAM5-HAM~~MAECHAM5-HAM

Elizaveta Malinina^{1*}, Alexei Rozanov¹, Ulrike Niemeier², Sandra Wallis³, Carlo Arosio¹, Felix Wrana³, Claudia Timmreck², Christian von Savigny³, and John P. Burrows¹

¹Institute of Environmental Physics (IUP), University of Bremen, Bremen, Germany

²Max-Planck Institute for Meteorology, Hamburg, Germany

³Institute of Physics, University of Greifswald, Greifswald, Germany

* now at the Canadian Centre for Climate Modelling and Analysis (CCCma), Environment and Climate Change Canada, Victoria, Canada

Correspondence: Alexei Rozanov (alex@iup.physik.uni-bremen.de)

Abstract. Stratospheric aerosols are an important component of the climate system. They not only change the radiative budget of the Earth but also play an essential role in ozone depletion. ~~Most noticeable those effects are~~ These impacts are particularly noticeable after volcanic eruptions when SO₂ injected with the eruption reaches the stratosphere, oxidizes and forms stratospheric aerosol. There have been several studies, where a volcanic eruption plume and the associated radiative forcing were analyzed using climate models. ~~Besides, volcanic eruptions were studied using the and/or~~ data from satellite measurements; ~~however, studies combining both models and measurement data are rare.~~ However, few have compared vertically and temporally resolved volcanic plumes using both measured and modelled data. In this paper, we compared changes in the stratospheric aerosol loading after the 2018 Ambae eruption observed by satellite remote sensing measurements and simulated by a global aerosol model. We use vertical profiles of the aerosol extinction coefficient at 869 nm retrieved at IUP Bremen from OMPS-LP (Ozone Mapping and Profiling Suite - Limb Profiler) observations. Here, we present the retrieval algorithm as well as a comparison of the obtained profiles with those from SAGE III/ISS (Stratospheric Aerosol and Gas Experiment III onboard International Space Station). The observed differences are within 25% for the most latitude bins, which indicates a reasonable quality of the retrieved limb aerosol extinction product. The volcanic plume evolution is investigated using both monthly mean aerosol extinction coefficients and 10-day averaged data. The measurement results were compared with the model output from ~~ECHAM5-HAM~~MAECHAM5-HAM, or ECHAM for short. In order to simulate the eruption accurately, we use SO₂ ~~injections~~ injection estimates from OMPS and OMI for the first phase of eruption and TROPOMI for the second phase. Generally, the agreement between the vertical and geographical distribution of the aerosol extinction coefficient from OMPS-LP and ECHAM is quite remarkable, in particular, for the second phase. We attribute the good consistency between the model and the measurements to the precise estimation of injected SO₂ mass and height as well as ~~through to the~~ nudging to ECMWF ERA5 reanalysis data. Additionally, we compared the radiative forcing (RF) caused by the increase of the aerosol loading in the stratosphere after the eruption. After accounting for the uncertainties from different RF calculation methods, the RFs from

ECHAM and OMPS-LP agree quite well. We estimate the tropical (20° N to 20° S) RF from the second Ambae eruption to be about -0.13 W/m^2 .

Copyright statement. TEXT

25 1 Introduction

The importance of stratospheric aerosols in the climate system is now well established. Stratospheric aerosols influence it both directly and indirectly. Firstly, they change the radiative budget of the Earth by scattering back to space the incoming shortwave solar radiation and, thereby, cause a net negative radiative forcing (RF) (see, e.g., Thomason and Peter, 2006; Kremser et al., 2016, and references therein). Secondly, stratospheric aerosols influence climate indirectly by participating in
30 chemical reactions which lead to ozone depletion (see, e.g., Solomon, 1999; Ivy et al., 2017; WMO, 2018).

Aerosols are present in the stratosphere all the time. Even though there is some evidence of a presence of organic particles, soot, meteoritic dust as well as other solid particles in the stratosphere, the most abundant are the droplets of sulfuric acid with a commonly assumed weight percentage of 75% H_2SO_4 and 25% H_2O . In the background state, stratospheric aerosols are formed by continuous emissions of carbonyl sulfide (OCS), dimethyl sulfide (DMS) and other sulfuric gases from the ocean surface (Kremser et al., 2016). However, occasionally this state is perturbed. In recent years due to
35 the increasing number of extreme weather events, biomass burning became a significant source of stratospheric aerosols. Thus, during large biomass burning events, like such as the Australian Bushfires of 2009 (Siddaway and Petelina, 2011) and 2019 (Siddaway and Petelina, 2011) (Khaykin et al., 2020), as well as the Canadian Wildfires of 2017 (Khaykin et al., 2018; Bourassa et al., 2019; Kloss et al., 2019), sulfuric gases and other combustion products are transported into the strato-
40 sphere by convective clouds (pyrocumulonimbus) (Fromm et al., 2010). Another noticeable source of stratospheric sulfur is anthropogenic fossil fuel combustion in South East Asia, where the aerosol precursors are transported into the stratosphere with the Asian Monsoon (Randel et al., 2010). Although these sources along with quiescent volcanic degassing are undoubtedly important, the large scale changes to the stratospheric aerosol layer are primarily driven by moderate and large volcanic eruptions, which emit sulfur dioxide (SO_2) directly into the upper troposphere lower stratosphere (UTLS region
45 (e.g. Kremser et al., 2016, and references therein) region (e.g. Kremser et al., 2016; Pitari et al., 2016, and references therein)

Although volcanic eruptions are infrequent, they still significantly influence climate short and long-term. Consequently, it is essential to consider them in climate models. According to Solomon et al. (2011); Haywood et al. (2014); Schmidt et al. (2018, and references therein), it has been shown that climate models' simulations that neglect forcing from vol-
50 canic eruptions since the year 2000 tend to project a faster rate of global warming for the first 15 years of the 21st century than those models the simulations including this volcanic forcing. There are numerous global aerosol model studies of historic and more recent eruptions. For example, several papers focus on the June 1991 eruption of Mount Pinatubo

(Niemeier et al., 2009; Feinberg et al., 2019; Dhomse et al., 2020)(e.g. Niemeier et al., 2009; Feinberg et al., 2019; Dhomse et al., 2020)

55 . Some studies also evaluate more recent moderate and small eruptions of the 21st century (e.g. Haywood et al., 2010; Kravitz et al., 2010, 2011; Zhu et al., 2018; Lurton et al., 2018). Similarly, there are multiple studies which use measurement results to analyze the changes in stratospheric aerosol loading either after some event (e.g., volcanic eruptions or biomass burning events) (e.g., Siddaway and Petelina, 2011; Bourassa et al., 2019), or long term (e.g., Bingen et al., 2004; von Savigny et al., 2015; Malinina et al., 2018). However, the studies which directly compare modelled and measured aerosol parameters are quite rare. In the papers known to the authors, the monthly mean stratospheric aerosol optical depth (SAOD) was typically the parameter
60 used to compare models and measurements (e.g., Haywood et al., 2010; Kravitz et al., 2010, 2011; Lurton et al., 2018). Brühl et al. (2018) used data from two satellite platforms and compared the vertically resolved aerosol extinction coefficient (Ext) at different wavelengths with model data in the period from 2002 to 2012. However, they compared spatial averages and did not focus on the plume distribution from volcanoes, assessing agreement only in general terms.

There is only a limited number of methods to observe stratospheric aerosols, and the only option to obtain a global distribution of stratospheric aerosol profiles is to use space-borne measurements. While the first decade of the twenty-first century is known as the "golden era" of stratospheric observations with such instruments as the Stratospheric Aerosol and Gas Experiment (SAGE) II, SAGE-III/Meteor (Damadeo et al., 2013), the SCanning Imaging Absorption SpectroMeter for Atmospheric CHartographY (SCIAMACHY) (Gottwald and Bovensmann, 2011), the Global Ozone Monitoring by Occultation of Stars (GOMOS) (Bertaux et al., 2004) and the Michelson Interferometer for Passive Atmospheric Sounding (MIPAS)
70 (Fischer et al., 2008) being on-orbit, currently there is a very limited number of space-borne missions, which can be used to retrieve stratospheric aerosol information. At the time of writing, only the Optical Spectrograph and InfraRed Imager System (OSIRIS) (Llewellyn et al., 2004), the Cloud-Aerosol Lidar and Infrared Pathfinder Satellite Observations (CALIPSO) (Vernier et al., 2011), the Ozone Mapping and Profiling Suite (OMPS) and the SAGE-III onboard International Space Station (ISS) continue stratospheric aerosol measurements. At the same time, OSIRIS and CALIPSO launched in 2001 and 2006,
75 respectively, are now well beyond their intended lifetimes. Consequently, in this paper, in order to obtain stratospheric aerosol characteristics, we use data from the OMPS instrument.

Model intercomparison studies (e.g., Clyne et al., 2021) revealed strong differences between the results of the evolution of the volcanic cloud from different models. Aerosol microphysical processes are highly non-linear and e.g. differences in transport can result in quite different particle distribution and size. Similarly, differences in microphysical processes between
80 the models can have a strong impact on simulated forcing. Therefore, comparing model results with satellite products can lead to improvements of the model results, and in turn, model results can also help to improve satellite products.

The scope of our study is to investigate the similarities and differences of in how models and measurements show a volcanic plume evolution. For this reason, we use the time and altitude resolved Ext data retrieved from the limb viewing instrument OMPS-LP and the output from the ECHAM-MAECHAM5-HAM model. We also study the differences in the modeled
85 RF and that calculated from the measured data. Our study was conducted on the example of the 2018 Ambae eruption. This particular eruption was chosen because it was one of the strongest in the last decade; although, although it did not receive as much attention as Kilauea eruption earlier that year or the 2019 Raikoke eruption.

Ambae (or Aoba) island is located in the South Pacific in Vanuatu (15.39°S, 167.84°E); ~~being; and it is~~ a shield volcano with three lakes in its caldera. According to Moussallam et al. (2019, and references therein), the previous significant Ambae eruption happened about 350 years ago; ~~this information agrees. This information is consistent~~ with that from the Smithsonian Institution (2019), according to which the active period of 2017-2018 was the strongest ever for this volcano. This period started on the 6 September 2017 and lasted over a year ending on the 30 October 2018. The researchers divide the eruption into four phases (Moussallam et al., 2019); however, for the stratospheric aerosol community, the most ~~essential-important~~ are the third and the fourth phases, when SO₂ was injected above the tropopause. ~~Namely, the-The~~ third phase from mid-March to mid-April 2018, is associated with ash falls and acid rains, the largest SO₂ injection of the period occurred on the 6 April at 16-18 km altitude. However, the fourth phase in mid-July 2018 was more severe. Thus, on the 27 July 2018, along with ash, SO₂ was injected into the UTLS region (17 km). For consistency reasons, further in the text "the first" or "April eruption" refers to the third phase, and "the second" or "July eruption" defines the fourth phase.

The paper is structured as follows. In Sec. ~~??, the OMPS-LP instrument and its stratospheric aerosol retrieval algorithm-2~~ spaceborne instruments used in this study as well as the ECHAM model are presented. The ~~comparison of OMPS-observational datasets, including the estimation of SO₂ injection from the eruptions, OMPS-LP retrieval algorithm as well as the comparison of OMPS-LP data with the data from SAGE III/ISS can be found in Sec. ??.~~ ~~The OMPS-LP aerosol extinction climatology is described in Sec. ??.~~ ~~The aerosol extinction coefficient distribution retrieved from the measurements made by the-3.~~ The evolution of aerosol plume after Ambae eruption as seen by OMPS-LP instrument is presented in Sec. ~~??.~~ ~~The distribution of aerosol extinction coefficient as well as estimation of mass from Ambae eruption and modelled by ECHAM~~ is described in Sec. ~~??.~~ ~~Discussion of the results and the RF comparisons are presented in Sec. ??4,~~ in the Subsec. 4.1 our estimations on the RF after the eruption are presented. The conclusions of the paper are provided in Sec. 5.

2 ~~OMPS-LP Instruments and Ext retrieval algorithm model~~

~~There is only a limited number of methods to observe stratospheric aerosols, and the only option to obtain a global distribution of stratospheric aerosol profiles is to use space-borne measurements. While the first decade of the twenty-first century is known as the "golden era" of stratospheric observations with such instruments as the Stratospheric Aerosol and Gas Experiment (SAGE) II, SAGE-III/Meteor (Damadeo et al., 2013), the Scanning Imaging Absorption Spectrometer for Atmospheric Cartography (SCIAMACHY) (Gottwald and Bovensmann, 2011), the Global Ozone Monitoring by Occultation of Stars (GOMOS) (Bertaux et al., 2004) and the Michelson Interferometer for Passive Atmospheric Sounding (MIPAS) (Fischer et al., 2008) being on-orbit, nowadays there is a very limited number of space-borne missions, which can be used to retrieve stratospheric aerosol information. At the time of writing, only the Optical Spectrograph and InfraRed Imager System (OSIRIS) (Llewellyn et al., 2004), the Cloud Aerosol Lidar and Infrared Pathfinder Satellite Observations (CALIPSO) (Vernier et al., 2011), the Ozone Mapping and Profiling Suite (OMPS) and the SAGE-III onboard International Space Station (ISS) continue stratospheric aerosol measurements. At the same time, OSIRIS and CALIPSO launched in 2001 and 2006, respectively, are now well beyond their intended lifetimes. Therefore, in this paper, in order to obtain stratospheric aerosol characteristics, we use data from the OMPS instrument.~~

2.1 OMPS-LP

OMPS onboard Suomi National Polar-orbiting Partnership (SNPP) launched in late 2011 by NASA consists of three sensors: nadir mapper (NM), nadir profiler (NP) and limb profiler (LP) (Seftor et al., 2014). To retrieve information on stratospheric aerosols, only measurements from LP can be used.

125 OMPS-LP registers solar radiance scattered by the atmosphere. Unlike SCIAMACHY and OSIRIS, OMPS-LP does not use a diffraction grating; instead, a prism disperses the light on a two-dimensional CCD (charge-coupled device) detector, which registers the radiance simultaneously from all altitudes from 290 to 1000 nm with the spectral resolution from 1 nm to 30 nm depending on the wavelength (Jaross et al., 2014). The LP has three vertical slits; however, we use only the measurements from the central slit because of remaining pointing and stray-light issues on the side ones. Each slit registers vertically 105 pixels
130 with a 1.5 km instantaneous field of view of each detector pixel. The radiances are registered with a vertical sampling of 1 km at the tangent point. The lowest and the highest registered altitudes vary depending on the latitude and season; nevertheless, the altitude span from 5 to 80 km is constantly covered (Jaross et al., 2014).

2.2 OMPS-NM

As already mentioned in Sec. 2.1, OMPS-NM is one of the OMPS sensors on SNPP satellite. According to Flynn et al. (2014)
135 , OMPS-NM provides measurements every 0.42 nm from 300 to 380 nm with 1.0 nm full width at half maximum resolution using a single grating and a CCD array detector. The instrument's cross-track field of view is 110° , which covers ≈ 2800 km on the Earth's surface; the along-track slit width field of view is 0.27° . Usually, the measurements are combined into 35 cross-track bins (20 spatial pixels viewing 3.35° (50 km) at nadir, and 2.84° at $\pm 55^\circ$ cross-track dimensions for the fields of view). The along track resolution at nadir is 50 km obtained by using a 7.6 s reporting/integration period.

140 Though originally meant to be a total ozone column sensor, currently, on the NASA-GES DISC website (NASA GES DISC, 2021), there are following products from NM listed: aerosol index (AI), cloud pressure and fraction, as well as total columns of ozone (O_3), nitrogen dioxide (NO_2) (Yang et al., 2014) and sulphur dioxide (SO_2) (Carn et al., 2015).

2.3 SAGE III/ISS

Stratospheric Aerosol and Gas Experiment (SAGE) III on the International Space Station (ISS) started operating in early 2017
145 as a continuation of the SAM-SAGE data record. SAGE-III/ISS provides solar and lunar occultation, as well as limb-scatter measurements (Cisewski et al., 2014); however, for now, for stratospheric aerosol extinction coefficient retrievals, only solar occultation measurements are used. The principle of solar occultation is to measure solar irradiance attenuated by the Earth's atmosphere between the Sun and the instrument during each sunrise and sunset.

SAGE-III/ISS provides continuous measurements from 280 to 1040 nm with a spectral resolution from 1 to 2 nm depending
150 on the wavelength, which are registered on a 808×10 pixel CCD. Additionally, there is a near infrared photodiode centered at 1550 nm (McCormick et al., 2019, and references therein). The retrieved aerosol extinction coefficients are provided at 384.2, 448.5, 520.5, 601.6, 676, 756, 869.2, 1021.2, 1543.9 nm. According to Cisewski et al. (2014), the aerosol extinction coefficients

provided by NASA have 0.75 km vertical resolution. In the official NASA product, aerosol extinctions are provided in 0.5 km steps from 0 to 45 km. Due to the ISS orbit, the measurements are performed from 70° N to 70° S. It should be noted here that occultation measurements are very sparse in comparison to limb measurements. This is because for one orbit a solar occultation instrument can register one sunrise and one sunset, while a limb instrument does not have these limitations. For example, OMPS-LP provides 180 measurements per orbit, which drastically increases geographical sampling.

2.4 MLS

Aura, a satellite platform with several instruments on-board, was launched on the 15 July 2004 and continues to operate at the time of writing. Aura circles around the Earth 14 times a day at 705 km altitude in a sun-synchronous polar orbit with 98.2° inclination. One of the instruments on Aura is the Earth Observing System Microwave Limb Sounder, or MLS for short (Waters et al., 2006). MLS measures atmospheric parameters remotely by observing millimeter- and submillimeter-wavelength thermal emission as the instrument field of view is scanned through the atmospheric limb. The instrument consists of four radiometers operating at 118 GHz, 190 GHz, 240 GHz, 640 GHz and 2.5 THz, whose output is analysed by banks of filters. The instrument scans the atmosphere in the tangent height range from 0 to 95 km for GHz scan and from 0 to 154 km for THz scan (Waters et al., 2006). The measured profiles are spaced 1.5° (165 km) apart along the orbit track. From MLS observations profiles of OH, HO₂, H₂O, O₃, HCl, ClO, HOCl, BrO, HNO₃, N₂O, CO, HCN, CH₃CN, volcanic SO₂ and temperature as well as information on cloud ice and geopotential height are obtained. Most data points in retrieved from MLS profiles are spaced approximately 2.7 km in altitude (Pumphrey et al., 2015).

2.5 OMI

The Ozone Monitoring Instrument (OMI) is another instrument on the Aura platform (see Sec. 2.4). OMI, a nadir-looking spectrometer, provides measurements of solar radiance and irradiance in three spectral channels in the wavelength range from 270 to 500 nm with a spectral resolution from 0.42 to 0.63 nm depending on the channel (Levelt et al., 2006). OMI uses three two-dimensional CCDs, one for each channel to detect the spectral and spatial information simultaneously. The instrument has a wide field of view of 114° corresponding to the swath width of 2600 km, measures approximately 14 orbits a day and provides daily global coverage. Levelt et al. (2018) and references therein reported so-called OMI row anomaly, a phenomenon that affects the quality of the radiance data for all wavelengths in a specific viewing direction of the instrument. It is believed to be a stem from a damage in the isolation that blocks part of the instrument's field of view. Despite this issue, OMI provides high-quality atmospheric products, amongst others O₃, NO₂, SO₂, and formaldehyde (HCHO) total columns (Levelt et al., 2018).

2.6 TROPOMI

One of the newer European Space Agency (ESA) instruments designed for air quality monitoring, is the nadir-looking Tropospheric Monitoring Instrument (TROPOMI), the only payload onboard of Sentinel-5 Precursor (S5P) (Veefkind et al., 2012)

. The S5P, operating in a sun-synchronous orbit at 824 km, was launched on the 13 October 2017, and TROPOMI continues
185 operation by the time of writing (Fioletov et al., 2020). TROPOMI is a spectrometer, which registers backscattered solar light
in the UV and visible bands from 270 to 500 nm, the near-infrared (NIR) from 675 to 775 nm and the shortwave-infrared
(SWIR) band from 2305 to 2385 nm, with a resolution from 1 nm in the UV to 0.25 nm in the SWIR. The instrument images
a strip of the Earth on a two dimensional detector for a period of 1 s during which the satellite moves by about 7 km. This
strip has dimensions of approximately 2600 km in the direction across the track of the satellite and 7 km in the along track
190 direction (Veeckind et al., 2012). The instrument has fine spatial resolution of 3.5 km by 7 km, which improved to 3.5 km by
5.5 km after August 2019. There are several species retrieved from TROPOMI including total columns of O_3 , carbon monox-
ide (CO), HCHO, NO_2 , SO_2 and methane (CH_4); O_3 profiles can be also obtained from the instrument's measurements
(Mettig et al., 2021).

2.7 ECHAM

195 The volcanic eruptions in our study were modeled by MAECHAM5-HAM. ECHAM5 (Giorgetta et al., 2006) is a general
circulation model (GCM) which was used in the middle atmosphere (MA) version, a high top model version with maxi-
mum altitude at 0.01 hPa (about 80 km). The horizontal resolution was about 1.8° , spectral truncation at wave number 63
(T63) with 95 vertical layers up to 0.01 hPa. The large wave numbers of the model were nudged to ERA5 reanalysis data
(Hersbach et al., 2018) to achieve realistic wind and transport conditions.

200 Interactively coupled to ECHAM is the aerosol microphysical model HAM (Stier et al., 2005), which calculates the oxi-
dation of sulfur and sulfate aerosol formation, including nucleation, accumulation, condensation and coagulation processes.
A simple stratospheric sulfur chemistry was applied above the tropopause (Timmreck, 2001; Hommel et al., 2011). ECHAM
prescribes oxidant fields of OH, NO_2 , and O_3 on a monthly basis, as well as photolysis rates of OCS, H_2SO_4 , SO_2 , SO_3 , and
 O_3 . The sulfate was radiatively active for both SW and LW radiation and coupled to the radiation scheme of ECHAM. These
205 simulations use the model setup described in Niemeier et al. (2009) and Niemeier and Timmreck (2015). Hereafter we refer to
MAECHAM5-HAM as ECHAM.

3 Observational data

3.1 Estimation of SO_2 injection

In order to simulate the Ambae eruptions, as a first step the amount of SO_2 emissions and injection altitude should be deter-
210 mined. Although there are methods to retrieve SO_2 mass and altitude from nadir measurements, it is well known that these
methods do not allow to distinguish, if SO_2 was released into the stratosphere or into the upper troposphere (see e.g. Carboni et al., 2016)
. Carboni et al. (2016) suggest that the combination of limb and nadir instruments might give a better answer. For this reason,
in our work we used a combination of MLS (see Sec. 2.4) and nadir SO_2 products to determine the altitude and the mass of
 SO_2 injection.

215 To assess the Ambae SO₂ burden and plume location, combined OMI (Sec. 2.5) and OMPS-NM (Sec. 2.2) data were used
for the April eruption. Yet for the July eruption, data from TROPOMI (Sec. 2.6) was taken into consideration. We did not
use the same SO₂ satellite product for both eruptive episodes for two reasons. First, the TROPOMI data with a fine grid and
extensive coverage is publicly available from the early May 2018, thus missing the first eruption. Second, even though the
combined OMI and OMPS-NM dataset temporally covers both eruption phases, it contains spatial gaps, which results in a
220 less precise SO₂ mass assessment. Thus, the current choice provides a trade-off between the spatial coverage and overall data
availability.

For the injection altitude estimation, MLS SO₂ number density profiles and tropopause altitude were used. Using the plume
location from OMI/OMPS-NM and TROPOMI data (see below), the profiles collocated with the plumes for April and July 2018
were analyzed. Using this data, it was identified that on the 6 April and the 27 July, the volcanic SO₂ reached the stratosphere.
225 These days coincide with the information presented by Moussallam et al. (2019); Kloss et al. (2020); Smithsonian Institution (2019)
. The profiles for the eruption dates can be found in Appendix A1.

3.1.1 Combined OMI and OMPS-NM dataset

For the first eruption, OMI SO₂ level 2 data with the assumption of an SO₂ distribution in the lower stratosphere (center of
mass altitude of 18 km (Li et al., 2017)) was used. Due to the OMI row anomaly (see Sec. 2.5), all rows > 21 (counting starts
230 at 0) were excluded. The first ten rows were discarded in order to limit the across-track pixel width (Fioletov et al., 2016), so
that only rows 10-21 were considered. Only the measurements obtained at solar zenith angles less than 70° were used. SO₂
total columns with large negative values below -1×10^{30} DU were not included in the analysis. After converting the data from
DU to g/m², a threshold of 0.05 g/m² (1.75 DU) was introduced to distinguish the volcanic signal from the background. All
satellite pixels that fulfilled the above requirements were averaged for each segment of the self-defined grid (see below). The
235 SO₂ mass loading in g/m² was multiplied with the segment area to obtain the SO₂ mass in units of g for every grid segment.
All orbits measured on one day were combined so that the SO₂ mass in each segment for a specific day was determined.

OMPS-NM level 2 data with the SO₂ column for the lower stratosphere (16 km) was used accordingly. Pixels at the edges of
the swath were discarded, excluding rows < 2 and rows > 33 (counting starts at 0) (Fioletov et al., 2020; Zhang et al., 2017)
. Only data with a pixel quality flag equal to 0 and a solar zenith angle less than 84° were used. Again, the SO₂ data was
240 converted from DU to units of g/m² and a threshold of 0.05 g/m² was applied before the pixels were averaged for each grid
segment and the SO₂ mass per day for each grid segment was determined as described above for the OMI data.

The daily OMI and OMPS data were projected on a self-defined grid with a resolution of 0.5° and averaged for each segment.
The grid dimensions were chosen from 150°E to 140°W and 10°N to 45°S for the April eruption. The data was summed up
over the entire grid to determine the total SO₂ mass for each day in this area. The results for the period from the beginning of
245 March until the end of April 2018 are presented in the panel (a) of Fig. 1 with the blue line. The estimate for the day when SO₂
reached the stratosphere is marked with a red circle. The daily data coverage in %, or the percentage of the self-defined grid
that contains data that could be used for the analysis, is depicted on the same panel with the grey line. Due to the large data
gaps, this SO₂ mass is a minimum estimate for the SO₂ injected during the eruption.

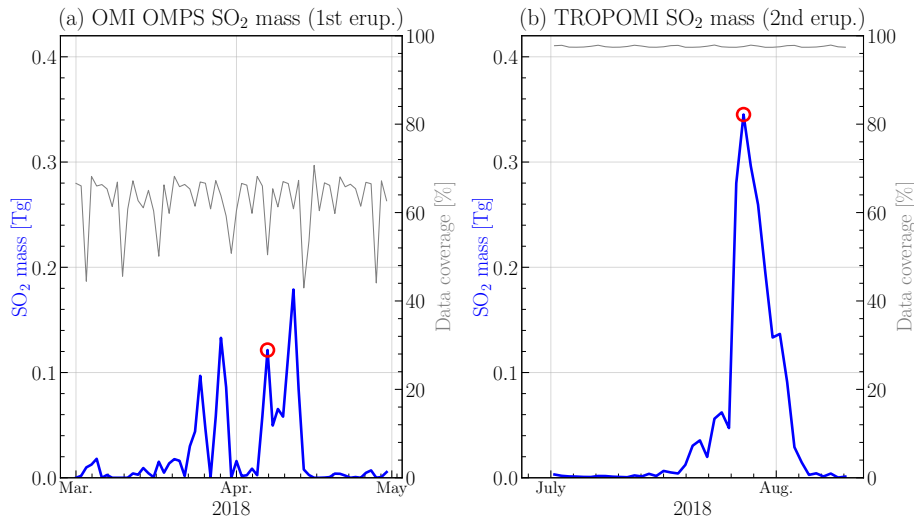


Figure 1. The SO_2 mass calculated for a threshold of 0.05 g/m^2 from the combined OMI and OMPS-NM for the first Ambae eruption in April (a) and from TROPOMI data for the July eruption (b).

The largest source of error for estimating the SO_2 emission is probably the choice of the assumed SO_2 profile, because the vertical distribution of the SO_2 affects the air mass factor used for the retrieval of the vertical column densities.

3.1.2 TROPOMI dataset

The SO_2 mass emitted during the eruption of Ambae in late July of 2018 was estimated by analyzing SO_2 total vertical columns from the TROPOMI instrument (see Sec. 2.6). A grid with a resolution of 0.1° in both longitude and latitude was defined from 10°N to 35°S and 150°E to 140°W . The utilized sulfur dioxide total vertical columns assuming an SO_2 profile represented by a 1 km thick box filled with SO_2 and centered at 15 km altitude, in order to model conditions in an explosive eruption (Theys et al., 2017). Only vertical column densities with values less than 1000 mol/m^2 were considered for the analysis. The data above this threshold was excluded because it was considered unrealistic and erroneous. Furthermore, a solar zenith angle less than 70° (for the SO_2 products that use an SO_2 box profile) or a quality value greater than 0.5 (for the SO_2 product that uses TM5 model profile), respectively, was required (Theys et al., 2020). TM5 model is a global chemical transport model that provides a daily forecast of SO_2 profiles (Theys et al., 2017). The total vertical column was multiplied by the SO_2 molar mass to get the SO_2 mass loading in the units of g/m^2 . Afterwards, similarly to Sec. 3.1.1, a threshold of 0.05 g/m^2 was applied and the SO_2 mass in units of g for every grid segment was calculated. Since some orbits overlap, 14 consecutive orbits covering a time span of approximately 24 h were bundled to a dataset batch and averaged for each grid segment. Finally, the SO_2 masses in all grid segments in the batch are summed up to obtain the total SO_2 burden.

The SO_2 masses calculated for every batch and for the thresholds of 0.05 g/m^2 during the Ambae eruption are presented in the panel (b) in Fig. 1. The date represents the date of the first orbit in each batch that intersects with the area of interest. With

the red circle, the day SO₂ reached the stratosphere according to MLS data is marked, while the data cover is depicted with grey line. The SO₂ mass increased to a maximum of 0.35 Tg on the 27 July and declined by the 5 August to magnitudes of Gg. The SO₂ mass for a threshold of 0 g/m² (not shown) exhibits a high SO₂ background of 0.1-0.15 Tg that quickly increases to a maximum of 0.51 Tg on the 27 July and decreases to 0.1 Tg on the 5 August. The application of a threshold of 0 g/m² seems to suggest an SO₂ background of approximately 0.1-0.15 Tg that is not apparent in Fig. 1, using a more restrictive threshold. Focusing only on the additional SO₂ entry, i.e. the difference between the maximum SO₂ and the background emission of 0.1-0.15 Tg, a total burden of approximately 0.35-0.4 Tg SO₂ was emitted applying a threshold of 0 g/m². This result is comparable to the maximal SO₂ burden in Fig. 1.

Furthermore, the calculated maximum of emitted SO₂ mass strongly depends on the SO₂ data product used. As mentioned in Sec. 3.1.1, the vertical SO₂ distribution affects the air mass factor that is used to retrieve the vertical column densities. Assuming a threshold of 0.05 g/m² and an SO₂ profile with the SO₂ existing in a 1 km thick box at an altitude of 15 km, as discussed above, results in the maximal SO₂ mass of 0.35 Tg. This value increases respectively to 0.5 Tg and even to approximately 1.3 Tg by assuming, respectively, a 1 km thick box at an altitude of 7 km and a profile from the TM5 model. These results emphasize the importance of an accurate assumption for the vertical SO₂ distribution (see Appendix B).

3.2 OMPS-LP *Ext* retrieval algorithm

As it can be inferred from its name, initially, OMPS was designed to obtain ozone products, and in the instrument design, the UV-Vis parts of the spectrum were prioritized. As the prism dispersion is non-linear, the spectral resolution of the measurements at the wavelength longer than 500 nm degrades exponentially, reaching about 30 nm at 1000 nm. This results in the situation that the usual stratospheric aerosol extinction wavelength 750 nm, used by, e.g., SCIAMACHY and OSIRIS (Rieger et al., 2018), is not suitable, for use as OMPS-LP measurements around this wavelength are affected by the O₂-A absorption band. Thus, for the stratospheric aerosol extinction retrieval, instead of 750 nm, we ~~use~~-used the measurements at 869 nm (with a spectral resolution of 22 nm), because the spectral interval from 830 to 900 nm is absorption free.

Even though some aspects of our algorithm have been briefly described in Arosio et al. (2018) and Malinina (2019), here, we provide a consolidated summary. The OMPS V1.0.9 aerosol extinction coefficient at 869 nm (*Ext*₈₆₉) retrieval algorithm was adapted from the SCIAMACHY V1.4 algorithm (Rieger et al., 2018) and uses the same regularized iterative approach. However, here, we ~~use~~-used the first-order Tikhonov regularization with the parameter value of 50 to smooth spurious oscillations in the level 1 V2.5 data. ~~Based on~~-Using the information provided by NASA, the signal-to-noise ratio (SNR) is set to 500 for all ~~the~~-tangent altitudes.

In V1.0.9, *Ext*₈₆₉ is retrieved on a regular 1 km grid from 10.5 to 33.5 km, with the measurement at 34.5 km being used as the reference. Additionally, the effective Lambertian albedo is simultaneously retrieved using the sun-normalized spectrum at 34.5 km. The retrieval is done under the assumption of stratospheric aerosols being spherical sulfate droplets (75% H₂SO₄ and 25% H₂O) with 0% relative humidity and unimodal lognormal particle size distribution. In this distribution the median radius (*r_{med}*) is equal to 0.08 μm and σ=1.6; the particle number density a priori profile ~~is~~-was chosen in accordance with the Extinction Coefficient for STRatospheric Aerosol (ECSTRA) background climatology (Fussen and Bingen, 1999). We ~~use~~

used the refractive indices from the OPAC database (Hess et al., 1998), for the selected wavelength the refractive index equals $1.425-1.38597 \times 10^{-7}i$. The stratospheric aerosol profile is defined from 10 to 46 km; below and above, the number density profile is set to 0. After the retrieval, the Ext_{869} values higher than 0.1 km^{-1} are considered to be cloud contaminated and thus are filtered. Here we want to highlight that we increased our threshold extinction value for the identification of cloud contamination (Malinina, 2019), because the previous threshold was filtering some profiles with increased aerosol loading.

4 ~~OMPS extinction comparison with SAGE III/ISS~~

3.1 ~~SAGE III/ISS instrument~~

~~Stratospheric Aerosol and Gas Experiment (SAGE) III on the International Space Station (ISS) started operating in early 2017 as a continuation of the SAM-SAGE data record. SAGE III/ISS provides solar and lunar occultation, as well as limb-scatter measurements (Cisewski et al., 2014); however, for now, for stratospheric aerosol extinction coefficient retrievals, only solar occultation measurements are used. The principle of solar occultation is to measure solar irradiance attenuated by the Earth's atmosphere between the Sun and the instrument during each sunrise and sunset. The solar occultation measurements are self-calibrating, and unlike limb instruments, for the Ext retrieval, no assumptions on the aerosol particle size distribution are needed, thus, making occultation measurements rather precise.~~

~~SAGE III/ISS provides continuous measurements from 280 to 1040 nm with spectral resolution from 1 to 2 nm depending on the wavelength, which are registered on a 808×10 pixel CCD. Additionally, there is an infrared photodiode centered at 1550 nm (McCormick et al., 2019, and references therein). According to Cisewski et al. (2014), the aerosol extinction coefficients provided by NASA have 0.75 km vertical resolution. In the official NASA product, aerosol extinctions are provided in 0.5 km steps from 0 to 45 km. Due to the ISS orbit, the measurements are performed from 70° N to 70° S . It should be noted here that occultation measurements are very sparse in comparison to limb measurements. This is because for one orbit a solar occultation instrument can register one sunrise and one sunset, while a limb instrument does not have these limitations. For example, OMPS-LP provides 180 measurements per orbit, which drastically increases geographical sampling.~~

3.1 Comparison of OMPS-LP and SAGE III/ISS

The OMPS-LP Ext_{869} was originally retrieved to improve the ozone product (Arosio et al., 2018); however, it can also be used to evaluate the changes in stratospheric aerosol loading after volcanic eruptions and biomass burning events (Malinina, 2019). Here, it should be noted that there are three other OMPS aerosol extinction products. Two of them are the official NASA Ext_{675} products V1.0 (Loughman et al., 2018) and V1.5 (Chen et al., 2018). Moreover, at the University of Saskatchewan, as a part of the ozone retrieval, a tomographic Ext_{750} product was obtained (Bourassa et al., 2019). All four Ext products were retrieved at different wavelengths and using different approaches. Thus, their **inter-comparison will be challenging-comparison will be not trivial** and will contain uncertainties, e.g., associated with Ångström-ngström exponent calculations.

In order to evaluate the quality of our Ext_{869} , it was compared with the SAGE III/ISS solar occultation product. There are several advantages to this comparison. Firstly, SAGE III is an independent data set; thus, ~~the OMPS instrumental uncertainties possible OMPS instrumental issues~~ (e.g. scattering angle dependency) will ~~not influence be revealed by~~ the comparison, ~~as it would be with which~~ would not be the case ~~for the when using~~ other OMPS products. Secondly, SAGE III is an occultation instrument, which means that its Ext profiles are rather precise and independent of the aerosol PSD assumption, ~~asin contrast to, e.g., OSIRIS. The solar occultation measurements are self-calibrating, and unlike limb instruments, for the Ext retrieval, no assumptions on the aerosol particle size distribution are needed, thus, making occultation measurements rather precise.~~

Another advantage of the comparison with SAGE III is the same measurement wavelength. Both ~~OMPS-LP and SAGE III~~ provide measurements at 869 nm, so ~~aerosol extinction does not need to be recalculated assuming an Ångström exponent no~~ conversion of the aerosol extinction to any other wavelength needs to be done. Even though the spectral resolution of the instruments at this wavelength is different (1.5 nm in SAGE III versus 30 nm in OMPS-LP), it does not influence the aerosol extinction coefficient strongly because the wavelength interval from 830 to 900 nm is absorption free.

For the comparison, individual profiles from ~~the~~ 07 June 2017 until ~~the~~ 31 August 2019 were used. The profiles were collocated using the following criteria, the difference between the profile's coordinates should be less than 2.5° in latitude, 10° in longitude and 24 hours in time. ~~The minimal time difference between profiles was 01:47:37, while the maximum difference is 22:07:38.~~ Overall, there are 19264 collocated measurements used for this comparison. For SAGE III data, ~~the same as for similarly to~~ OMPS, the aerosol extinction values higher than 0.1 km^{-1} were filtered out. Additionally, the SAGE III Ext_{869} values were excluded, if the uncertainty provided by NASA is higher than 50%. We did not filter negative Ext_{869} because this would bias the comparison (see Damadeo et al. (2013) for details).

The mean relative differences between OMPS and SAGE III Ext_{869} are presented in Fig. 2 in 20° latitude bins. For most of the altitudes in all latitude bins, the relative difference is within 25%. In the tropical and mid-latitudes, the only exceptions are the altitudes below 18 km, where despite filtering, the influence of clouds is still present. The largest differences are observed in high latitudes (40° to 80° in both hemispheres), in particular, at the altitudes above 24 km. For example, at about 28 km altitude, the differences reach up to 60% in these latitude bins.

Generally, the above-described differences are similar to the relative differences between SCIAMACHY V1.4, OSIRIS v5.07 and SAGE II v7 (Rieger et al., 2018; Malinina, 2019). Additionally, Chen et al. (2019) showed that the differences seen between OMPS Ext_{675} V1.5 and SAGE III product have the same shape and order of magnitude. Rieger et al. (2018) studied precisely the reasons for the ~~seen-observed~~ differences. Since the OMPS V1.0.9 algorithm is very similar to the SCIAMACHY V1.4 algorithm used in that study, and since the OMPS and SCIAMACHY have very similar geometries, the same explanations as Rieger et al. (2018) are appropriate. ~~Thus~~ According to this study, the most important sources of errors in limb retrievals arise from the uncertainly assumed aerosol loading at the reference tangent altitude as well as the unknown aerosol particle size distribution parameters. The latter factor mostly affects the high latitudes where the viewing geometries are close to forward and backward scattering.

Based on our comparison and the results from the other limb-occultation instrument studies, it can be concluded that our OMPS V1.0.9 Ext_{869} is of sufficient quality to be used for scientific purposes.

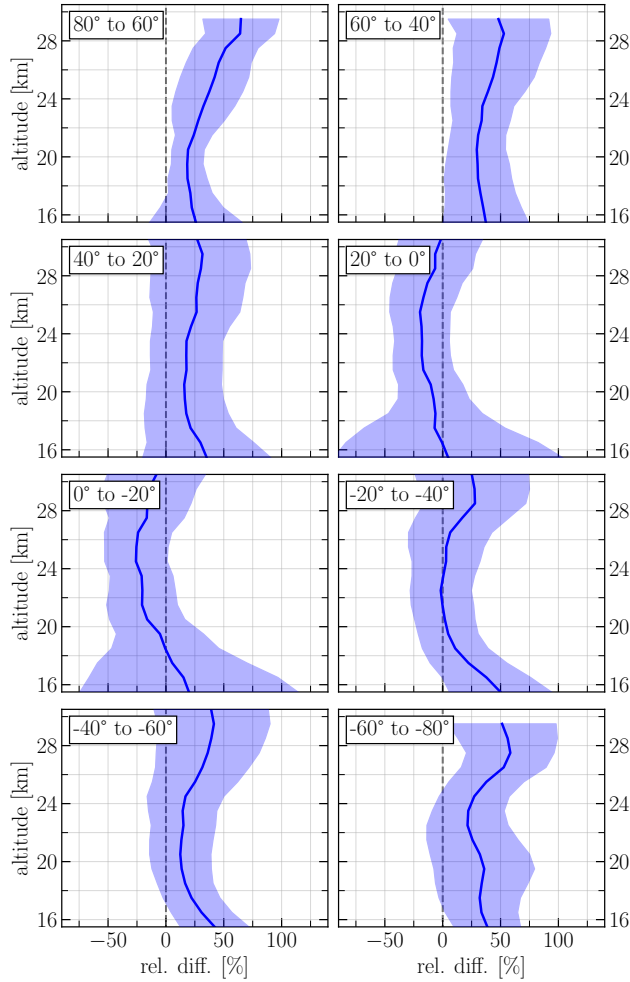


Figure 2. Mean relative difference in Ext_{869} between OMPS-LP and SAGE III/ISS, calculated as $200 \times (\text{OMPS} - \text{SAGE}) / (\text{OMPS} + \text{SAGE})$. The shaded areas show ± 1 standard deviation.

4 OMPS-LP aerosol extinction climatology

3.1 OMPS-LP aerosol extinction climatology

In order to study the aerosol extinction coefficient evolution after a volcanic eruption, the OMPS V1.0.9 product has to be averaged in some fashion. We have created two level 3 products, which are monthly and 10-day averaged Ext_{869} . Both products were ~~put~~ binned onto a regular geographical grid with 2.5° latitude and 5° longitude steps. Since the retrieved product is provided on the regular 1-km grid, no vertical averaging is needed.

An example of zonal monthly mean Ext_{869} averaged in 30° latitude bins for the whole OMPS operation period is presented in Fig. 3. In this figure, the volcanic eruptions and a relevant biomass burning event are shown with grey triangles with numbers.

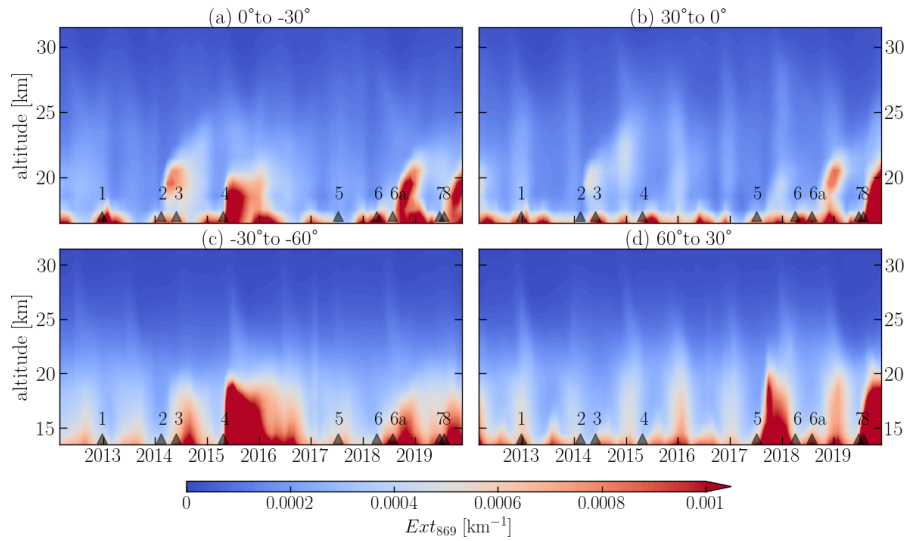


Figure 3. Monthly mean aerosol extinction coefficient (Ext_{869}) distribution with as a function of time and altitude. Ext_{869} was retrieved from OMPS-LP measurements. The values were obtained by binning and averaged over longitude in 30° latitude bins zonally averaging OMPS-LP monthly level 3 Ext_{869} . The triangles with numbers represent volcanic eruptions and biomass burning events (see Tab. 1).

Table 1. Volcanic eruptions and biomass burning events shown in Fig. 3.

Number	Volcano	Date of the eruption	Latitude	Longitude
1	Copahue	23 Dec. 2012	-37.51	-71.1
2	Kelut	13 Feb. 2014	-7.55	112
3	Sangeang Api	30 May 2014	-8.2	119.07
4	Calbuco	22 Apr. 2015	-41.19	-72.37
5	Canadian Wildfires	July-Aug. 2017	51.64	-121.3
6	Ambae	06 Apr. 2018	-15.4	167.84
6a		27 July 2018		
7	Raikoke	22 June 2019	48.3	153.4
8	Ulawun	26 July 2019	-5.05	151.33

The information on the volcanic eruptions is presented in Tab. 1. We show only Ext_{869} within 60° in both hemispheres because, as it was pointed out in Sec. 3.1, the aerosol extinctions above these latitudes are associated with larger uncertainties. Furthermore, the main scope of this paper is to study the tropical Ambae eruptions; thus, we do not focus our attention on aerosol loading in the high latitudes.

Analysis of Fig. 3 shows that there is a certain increase of Ext_{869} in the very beginning of OMPS operation in the Northern Hemisphere latitude bins in the bin between 60° and 30° . This is associated with the eruption of Nabro (13° N) in the middle of

380 2011. Additionally, one can see an increase of Ext_{869} some time after eruptions from Table 1 and from Canadian Wildfires of
2017 (number 5 in Fig. 3 and Table 1). The degree of the enhancement, as well as the time lag between the eruptions, seen in the
latitude bands, are dependent on the volcano's location and the eruption strength. Usually, for the tropical eruptions, an increase
in stratospheric aerosol loading is seen globally, because the aerosols and precursors are transported with the Brewer-Dobson
Circulation (BDC) to both hemispheres. Also, in the tropics, the BDC is responsible for the tape recorder effect, or delayed
385 increase in Ext_{869} with ~~the height~~ height (Vernier et al., 2011). For example, in Fig. 3 (a) and (b), the tape recorder effect is
seen for the Kelut, Sangeang Api, Calbuco and Ambae eruptions as well as for the Canadian Wildfires. For the eruptions in the
mid-latitudes, the increase usually stays in the hemisphere where it occurred (e.g., Oman et al., 2006; von Savigny et al., 2015;
Toohey et al., 2019; Malinina, 2019).

Another ~~noticeable~~ readily identifiable feature in Fig. 3 is the periodical increase of Ext in all latitude bins. There are
390 several factors causing this pattern. For the tropical region, there is a periodic signal above 25 km altitude associated with
the quasi-biennial oscillation (QBO). The ~~influence of~~ years, when the QBO results in an increase of Ext_{869} in the panel (a)
are 2013, 2015 and 2017; for panel (b), these years are 2012, 2014 and 2017. Here, it is important to mention, that during
the OMPS operation period, two QBO disruptions were reported, namely in 2015/2016 (Newman et al., 2016) and 2019/2020
(Kang and Chun, 2021). These disruptions might somewhat mask the increases in the high-altitude extinctions. Generally, the
395 influence of the QBO on stratospheric aerosols was previously reported by e.g. Hommel et al. (2015); Brinkhoff et al. (2015);
von Savigny et al. (2015); Malinina et al. (2018). Additionally, the annual seasonality, which is seen as yearly re-occurring
lighter coloured stripes, in both tropics and mid-latitudes is related to two factors. First, there are some yearly changes in
stratospheric aerosol loading (Hitchman et al., 1994; Bingen et al., 2004). ~~But~~ Second, for the limb viewing instruments, ~~the~~
~~more-an~~ important factor is the seasonality in solar scattering angle, which leads to artifacts of the retrieval predominately in
400 the extratropical regions (see e.g. Rieger et al., 2018).

One should also mention the increase in the extinction at approximately 16.5-17 km in the panels (a) and (b), and at around
13.5-15 km in the panels (c) and (d). These are the residual clouds, which were not filtered by our threshold. Though we show
the data in Fig. 3 above the average tropopause height for the bin, some overshooting convective clouds still could be present and
influence an average Ext . Here we want to highlight, that we are aware of disadvantages of our fixed cloud filtering threshold,
405 which can also be considered quite high. As we state above in Sec. 3.2, our previous threshold was too low and was filtering out
parts of volcanic and forest fires plumes. Furthermore, any fixed threshold would either filter out some high extinction events,
or leave some fractions of cloud in. However, the other commonly used cloud filtering approach exploiting altitude derivative
of spectral ratio also suffers from poor discrimination under certain conditions (Chen et al., 2016; Rieger et al., 2019).

4 ~~Aerosol extinction coefficient evolution after Ambae eruption~~ as seen by OMPS-LP

410 4.1 Aerosol extinction coefficient evolution

As it was ~~already~~ highlighted in the introduction, Ambae was one of the largest eruptions of the last decade but has not been
a focus of scientific or public interest. The eruptive period, which lasted over a year, had two explosive phases when SO_2

was injected into the stratosphere (the exact information on SO₂ mass estimation can be found in Sec. 3.1). The first emission was smaller, and the perturbation in Ext_{869} did not reach the altitudes above 21 km (see Fig. 3 (a) and (b)). The second emission was considerably larger; it perturbed Ext_{869} up to 23.5 km in the tropics and up to 22 km in the extratropical regions. ~~Although~~ However, to better evaluate the plume evolution, we will further analyze 10-day averaged Ext_{869} .

~~Evolution of the aerosol extinction coefficient (Ext_{869}) at 18.5 and 20.5 km altitude after Ambae eruptions of 2018. In panels (a) and (b) Ext_{869} was retrieved from OMPS-LP measurements; for panels (c) and (d) Ext_{869} was modelled by ECHAM-HAM. Both datasets were averaged over 10 day period.~~

420 4.1.1 Ambae eruption as seen by OMPS-LP

The evolution with time and altitude of the 10-day averaged zonal mean Ext_{869} averaged over longitudes at 18.5 and 20.5 km is presented in panels (a) and (b) of Fig. 4. Foremost, it should be noted that the increase of Ext_{869} in February – May 2018 in the latitudes above 25°N at 18.5 km and above 7°N at 20.5 km is related to the disappearing plume from the Canadian Wildfires of 2017. ~~The first~~ Already in the first week after the eruption a small increase in Ext_{869} associated with the April Ambae eruption ~~appears at 18.5 km in the first week after the injection.~~ is seen around the Ambae location; however, this increase cannot be uniquely attributed to the Ambae eruption and can be caused by the transport of the aerosol from preceding events. The more significant increase is observed in early May 2018. At the time, the plume is located around 10–25°S and stays there until late June. In June, the increase in Ext_{869} starts to spread to the south, reaching 35–45°S in July 2018. At 20.5 km, the increase after the first SO₂ release is rather negligible. Nevertheless, there is still an area with the increased aerosol loading below 20°S from the beginning of May.

In late July 2018, at the fourth phase of the eruption, Ambae injected another portion of ash and SO₂. Almost at the same time, Ext_{869} increases at 18.5 km directly at the source. In about two weeks, the volcanic plume starts to spread both ~~northwards and southwards~~ northward and southward and is located between the equator and 35°S in early September, reaching 45°N in November – December 2018. The southern border of the plume at 18 km is harder to identify because it mixes with the aerosol from the previous SO₂ release. However, an increased aerosol loading is observed to the south of 35°S in September and intensifies further with the time. By mid October 2018, ~~the plume starts to vanish at 18.5 km,~~ the plume shows a clear reduction around the equator and continues to weaken with time. At 20.5 km, the plume appears in mid-September 2018 at around 10°S, spreads northwards and southwards from that moment on, reaching its maximum in November. It is located in between 30° S and 35° N in mid December 2018. Again, at the southern border of the plume, there is an area of increased Ext_{869} , which is related to both eruptions.

5 Ambae eruption modelled with ECHAM-HAM

4.1 Estimation of injection

4.0.1 Ambae eruption modelled by ECHAM

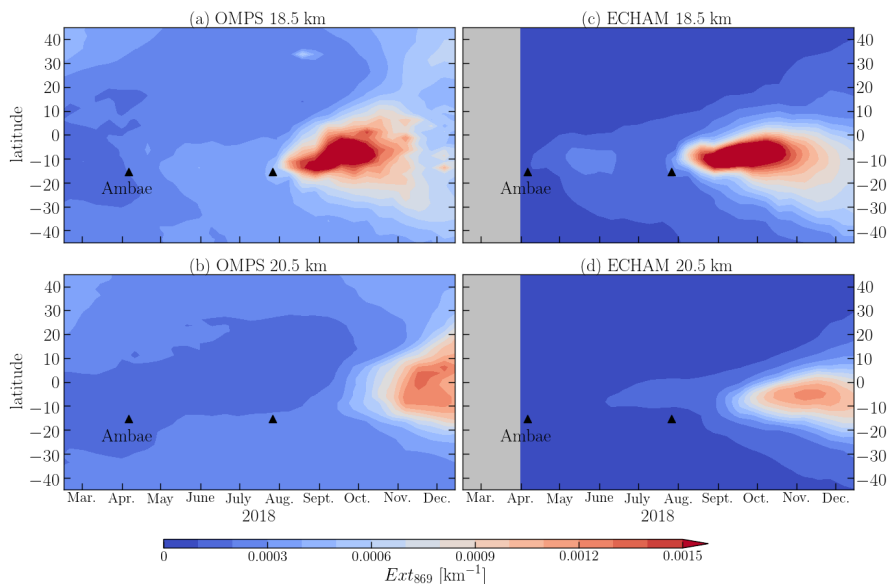


Figure 4. The evolution of the aerosol extinction coefficient (Ext_{869}) at 18.5 and 20.5 km altitude after the Ambae eruptions of 2018. In panels (a) and (b) Ext_{869} was retrieved from OMPS-LP measurements; for panels (c) and (d) Ext_{869} was modelled by MAECHAM5-HAM. Both datasets were averaged over 10 day periods.

~~In order to simulate the Ambae eruptions, as a first step the amount of~~ The Ambae experiment setup used the estimated
 445 ~~SO₂ emissions and injection altitude should be determined. Although there are methods to retrieve mass and altitude from~~
~~nadir measurements, it is well known these methods do not allow to distinguish, if was released into the stratosphere or~~
~~into the upper troposphere (see e.g. Carboni et al., 2016). Carboni et al. (2016) suggest that the combination of limb and nadir~~
~~instruments might give a better answer. For this reason, in our work we use a combination of MLS (Microwave Limb Sounder)~~
~~(Pumphrey et al., 2015) and nadir products to determine the altitude and the mass of injection.~~

450 ~~To assess the Ambae burden and plume location, combined OMI (Ozone Monitoring Instrument) (Fioletov et al., 2011)~~
~~and OMPS-NM (Carn et al., 2015) data were used for the April eruption. Yet for the July eruption, data from TROPOMI~~
~~(TROPOspheric Monitoring Instrument) was taken into consideration. We do not use the same satellite product for both eruptive~~
~~episodes because of two reasons. First, the TROPOMI data with a fine grid and extensive coverage is publicly available from~~
~~the early May 2018, thus missing the first eruption. Second, even though the combined OMI and OMPS-NM dataset temporally~~
 455 ~~covers both eruption phases, it contains spatial gaps, which results in less precise mass assessment. Thus, the current choice~~
~~provides a trade-off between the spatial coverage and overall data availability.~~

~~For the injection altitude estimation, MLS number density profiles and tropopause altitude were used. Using the plume~~
~~location from OMI/OMPS-NM and TROPOMI from Sec. 3.1 and the injection altitudes from MLS data (see below), the~~
~~profiles collocated with the plumes for April and July 2018 were analyzed. Based on that data, it was identified that on~~

460 the 6 April and the 27 July, the volcanic reached the stratosphere. These days coincide with the information presented by Moussallam et al. (2019); Kloss et al. (2020); Smithsonian Institution (2019).

4.0.2 Combined OMI and OMPS-NM dataset

For the first eruption, OMI level 2 data with the assumption of an distribution in the lower stratosphere (center of mass altitude of 18 km (Li et al., 2017)) was used. Due to the OMI row anomaly, all rows > 21 (counting starts at 0) were excluded. The first ten rows were discarded in order to limit the across-track pixel width (Lu et al., 2013), so that only rows 10-21 were considered. Furthermore, the radiative cloud fractions less than 0.2 and a solar zenith angle less than 70° were required. total columns with large negative values below $-1E30$ DU were not included in the analysis. A threshold of 0.05 g/m^2 was introduced to distinguish the volcanic signal from the background. All satellite pixels that fulfilled the above requirements were averaged for each segment of the self-defined grid (see below). The data was converted into units of g/m^2 and multiplied with the segment area to obtain the mass in units of g for every grid segment. All orbits measured on one day were combined so that the mass in each segment for a specific day was determined.

OMPS-NM level 2 data with the column for the lower stratosphere (16 km) was used accordingly. Pixels at the edges of the swath were discarded, excluding rows < 2 and rows > 33 (counting starts at 0) (Fioletov et al., 2020; Zhang et al., 2017). Only data with a pixel quality flag equal to 0 and a solar zenith angle less than 84° were used. Again, a threshold of 0.05 g/m^2 was applied, and the Appendix A). As pointed out, the result of the calculated SO_2 mass per day for each grid segment was determined as described above for the OMI data.

The daily OMI and OMPS data were projected on a self-defined grid from 10° N to 45° S and from 150° E to 140° W with a resolution of 0.5° and averaged for each segment. The data was summed up over the entire grid to determine the total mass for each day in this area. The results for the period from the beginning of March until the end of April 2018 are presented in the panel (a) of Fig. 1. The estimate for the day when reached the stratosphere is marked with a red circle. Due to the large data gaps, this mass is from OMI/OMPS data for the April eruption provides only a minimum estimate for the ejected during the eruption.

Before the 0.05 threshold was applied, the combined satellite measurements covered approximately 40–70% of the self-defined grid.

485 The largest source of error for estimating the emission is probably the choice of the assumed profile because the vertical distribution of the affects the air mass factor used for the retrieval of the vertical column densities.

The mass calculated for a threshold of 0.05 g/m^2 from the combined OMI and OMPS-NM for the first Ambae eruption in April (a) and from TROPOMI data for the July eruption (b).

4.1 TROPOMI dataset

490 The mass emitted during the eruption of Ambae in late July of 2018 was estimated by analyzing total vertical columns from the TROPOMI instrument (Veefkind et al., 2012) on the Copernicus Sentinel-5 Precursor satellite for the time period from the

1 July 2018 to the 29 September 2018. This instrument allows for global daily coverage of with a spatial resolution of 3.5×7 km.

495 A grid with a resolution of 0.1° in longitude and latitude, respectively, was defined from 10° N to 45° S and 150° E to 140° W. The utilized sulfur dioxide total vertical columns assuming an profile represented by 1 km thick box filled with and centered at 15 km altitude, in order to model conditions in an explosive eruption (Theys et al., 2017). Only vertical column densities with values less than 1000 mol/m^2 and a quality value greater than 0.5 were considered for the analysis (Pedernana et al., 2018). The total vertical column was multiplied by the molar mass to get the mass loading in the units of g/m^2 . Afterwards, a threshold of 0.05 g/m^2 was applied. The mass loadings exceeding the selected threshold were averaged in each grid segment, and the result multiplied by the segment area in order to obtain the mass in units of g for every grid segment. Since some orbits overlap, 500 14 consecutive orbits covering a time span of approximately 24 h were bundled to a dataset batch and averaged for each grid segment. Finally, the mass of the entire grid per batch are summed up to obtain the total burden.

The masses calculated for every batch and for the thresholds of 0.05 g/m^2 during the Ambae eruption are presented in the panel (b) in Fig. 1. The date represents the date of the first orbit in each batch that intersects with the area of interest. 505 With the red circle, the day reached the stratosphere according to MLS data is marked. The mass increased to a maximum of $0.36 \pm 0.04 \text{ Tg}$ on the 27 July and declined by the 5 August to magnitudes of Gg. The mass for a threshold of 0 (not shown) exhibits a high background of 0.2 Tg that is strongly increasing to a maximum of 0.57 Tg on the 27 July. It decreases to 0.15 Tg on the 5 August, before it goes back up to 0.27 Tg on the 14 August and decreases steadily afterwards. The application of a threshold of 0 seems to suggest an background of approximately 0.2 Tg that is not apparent in Fig. 1, using a more restrictive 510 threshold. Focusing only on the additional entry, i.e. the difference between the maximum and the background emission of 0.2 Tg , a total burden of approximately 0.4 Tg was emitted applying a threshold of 0. This result is comparable to the maximal burden in Fig. 1.

Furthermore, the calculated maximum of emitted mass strongly depends on the data product used. As mentioned in Sec. 3.1.1, the vertical distribution affects the air mass factor that is used to retrieve the vertical column densities. Assuming a threshold 515 of 0.05 and an profile with the existing in a 1 km thick box at an altitude of 15 km, as discussed above, results in the maximal because the analysis suffered from large data gaps. In accordance with Kloss et al. (2020), an SO_2 mass of 0.36 Tg . This value increases to 0.57 Tg and even to approximately 1.6 Tg by assuming a 7 km profile and a profile from the TM5 model, respectively, emphasizing the importance of a reasonable mass of 0.12 Tg was chosen as a realistic assumption for the vertical distribution.

520 4.1 Model experiment

The volcanic eruptions were modeled by MAECHAM5-HAM. ECHAM is a general circulation model (GCM) which was used in the middle atmosphere version of the GCM ECHAM5 (Giorgetta et al., 2006). The horizontal resolution was about 1.8, spectral truncation at wave number 63 (T63) with 95 vertical layers up to 0.01. The large wave numbers of the model were nudged to ERA5 reanalysis data (Hersbach et al., 2018) to achieve realistic wind and transport conditions.

525 ~~Interactively coupled to ECHAM is the aerosol microphysical model HAM (Stier et al., 2005), which calculates the oxidation of sulfur and sulfate aerosol formation, including nucleation, accumulation, condensation and coagulation processes. A simple stratospheric sulfur chemistry is applied above the tropopause (Timmreck, 2001; Hommel et al., 2011). The sulfate is radiatively active for both SW and LW radiation and coupled to the radiation scheme of ECHAM. These simulations use the model setup described in Niemeier et al. (2009) and Niemeier and Timmreck (2015). Hereafter we refer to MECHAM5-HAM as ECHAM.~~

530

~~The experiment setup used the estimated emissions from Sec. 3.1. We April eruption in the simulation. Thus, we injected 0.12 Tg SO₂ at altitudes of 82 to 102 hPa on the 6 April for four hours and 0.36 Tg SO₂ at altitudes between 74 and 90 hPa on the 27 July for 24 hours, starting at 18hUTC. UTC. During the review process, the extension of the self-defined grid for the TROPOMI analysis was reduced to exclude SO₂ artifacts at the borders which resulted in a slight decrease for the estimates~~
535 ~~SO₂ mass from 0.36 to 0.35 Tg. The ECHAM simulations were carried out with the former value, but we do not expect a significant impact due to that difference.~~ The long eruption phase was chosen to take the observed series of eruptions into account. To slow down the oxidation of SO₂ due to the limited availability of OH in a volcanic cloud (Mills et al., 2017), the concentration of OH was limited in the first days after the eruption: Day 1 to 10 to 40% and day 10 to 20 to 60% of the prescribed OH. The sea surface temperature (SST) is set to a climatological value (Hurrell et al., 2008).

540 In order to be consistent with OMPS-LP measurements, the output of ECHAM was interpolated to the same **altitudinal vertical** grid as provided by OMPS-LP. ECHAM provides *Ext* at 550 and 825 nm, thus, for the comparison consistency, the simulated *Ext* was recalculated to 869 nm and afterwards the 10-day averages were calculated.

4.1 ~~Aerosol extinction coefficient evolution after Ambae eruption as modelled by ECHAM~~

The simulated distribution of *Ext*₈₆₉ with time and latitude at 18.5 and 20.5 km is presented in panels (c) and (d) of Fig. 4. In
545 these panels, it is seen that at 18.5 km the aerosol extinction coefficient starts to increase almost right after the first eruption and reaches its peak in May. The **main-part-majority** of the volcanic aerosol stays in the tropics between 30° S and the equator. A small amount of aerosol is dispersed meridionally right after the eruption. After the second eruption, at the end of July, the first aerosol is formed right after the eruption with *Ext* increasing slowly until it reaches the maximum in September. Most **aerosol is aerosols are** located to the south of 10° N. In the last days of September, the plume is still very well pronounced and it starts
550 to spread meridionally, mostly southwards. By beginning of October *Ext* increases also in the Northern Hemisphere at 20° N, this increase spreads with the time to 40° in the late December. The plume starts to weaken in the beginning of November.

At 20.5 km the plume from the first eruption appears in late June. The plume at this altitude is quite weak and does not extend much over the latitudes. Basically, it is a small **blob-area** in between the equator and 10° S. The increase in *Ext* associated with the second eruption appears at 20.5 km in very late August, by the middle of September the plume intensifies and starts to
555 expand meridionally. It reaches its maximum by November, when the increase is seen from 10° N to 40° S. From that moment, the plume starts to slowly disappear. In late December, the *Ext* increase is seen from 30° N to 45° S.

5 Discussion

4.1 Aerosol extinction coefficient

4.0.1 Discussion

560 In order to evaluate the consistency of the results from OMPS and ECHAM, panels (a), (b) and (c), (d) of Fig. 4 need to be compared. It is obvious that the model and the observations are very close to each other, in particular, at 18.5 km. The plume from the first eruption appears and intensifies at the same time at 18.5 km; however, in the model, it is weaker, and it reaches 20.5 km about a month later. This is most likely related to the fact that in the model, neither the anthropogenic nor biomass burning sources are taken into account.

565 The Ambae plume from the July eruption looks even more similar in the model results and measurements. Not only the plume appears at the same time at 18.5 km and is located at the same latitudes, but also both model and measurements show a wave-shape of the plume. The curvature in both plumes appears in mid September, however, in the OMPS-LP data, the plume is bending stronger to the north. It should also be noted that the ECHAM simulations show a more intensive and longer living plume at this altitude. Additionally, in the OMPS-LP data, in the second part of October, the aerosols move evenly north- and
570 southward, while in the ECHAM data, the plume is transported rather to the south. In ECHAM data at 20.5 km, the July plume appears about two-three weeks earlier than in the OMPS measurements. Though the intensity of the modeled plume at this altitude is slightly weaker, the absolute differences are smaller than at 18.5 km. However, the horizontal distribution of the modeled plume is less consistent with the measurements. While the plume in ECHAM ~~data~~ stays with the time ~~at the same geographical location in the same latitude band~~ mostly in the Southern hemisphere, in the OMPS data, it has a C-shape around
575 the equator.

It should be highlighted that even though there are some differences between the modeled and measured Ext , the consistency is quite remarkable. There are ~~two~~ key main factors which contributed to this particular agreement between OMPS and ECHAM, namely, rather precise SO_2 mass and height estimation as well as nudging of meteorological data. ~~Thus~~ Consequently, it is seen that the second plume, whose emission was estimated from TROPOMI data, was modeled more accurately. At the
580 same time, our internal studies showed that the ECHAM SO_2 sensitivity plays a key role in the lifetime and distribution of the plume ~~-(see Figure in the Supplements)~~.

It is a well-known feature of ECHAM that the meridional transport is too strong, causing a relatively short lifetime of sulfate (e.g. Niemeier et al., 2009), especially compared to results of other models (e.g. Marshall et al., 2018). Therefore, the nudging of the meteorological data provided a realistic transport pattern resulting in good agreement with OMPS-LP measurements.
585 However, the nudging database, the ERA5 reanalysis, ~~is a model product~~ has not only observational, but also a strong model component as well. Thus, small differences ~~to~~ with observations are rather possible, especially in the stratosphere. Additionally, the stratospheric aerosol layer is close to the ozone layer at 24 km. ECHAM uses prescribed ozone and OH values, which do not change due to the presence of volcanic aerosol.

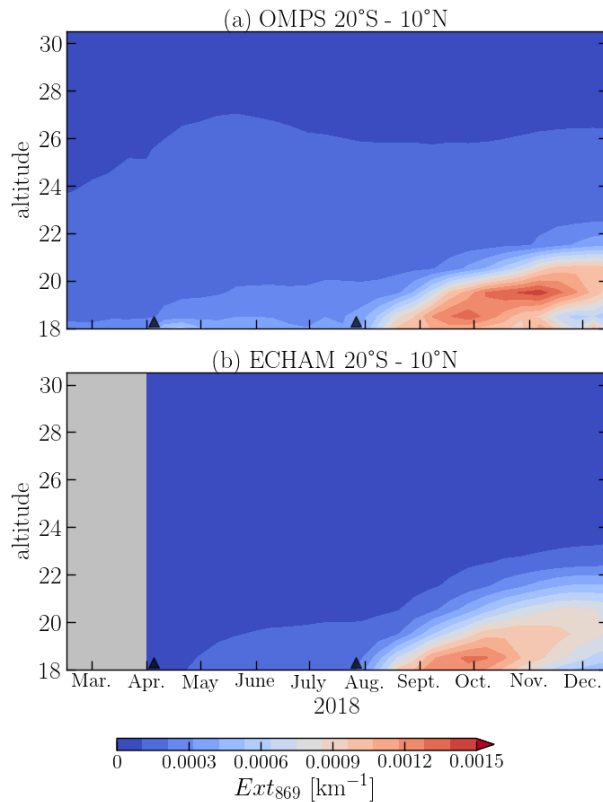


Figure 5. Evolution of zonal mean aerosol extinction coefficient (Ext_{869}) in the tropics (20°S – 20°N) with altitude and time after the Ambae eruptions of 2018. In the panel (a) the data from OMPS-LP is presented, in the panel (b) the simulation with ECHAM-MAECHAM5-HAM is plotted. Both datasets were averaged over a 10-day period.

Another way to assess the degree of consistency between the model and the measurements is to analyze the vertical distribution of Ext with the time (see Fig. 5). Since most of the plume stayed in the tropical region, for Fig. 5 the OMPS (panel (a)) and ECHAM (panel (b)) Ext were averaged between 20° S and 10° N. In this figure, it is again obvious that in the model the perturbation from the volcano reached the same altitudes. Additionally, it is seen-observed that the plume was weaker for the April eruption. However, consistency for the second eruption is again striking. Not only the The plume has the same overall shape, but it and is located at the same time coordinates, with the only exception of a slightly increased blob in the OMPS data at. A disagreement is seen, however, around the 19.5 km in November. Thus, vertical transport is slightly weaker in ECHAM, which explains some of the differences to the OMPS data in the horizontal cross-section at 20.5 km altitude in November, where OMPS-LP data show an increased extinction not present in ECHAM simulations. Also Kloss et al. (2020) report maximum extinction in 18-19 km layer in November when analyzing OMPS-LP data. The reasons for the observed disagreements are still under investigation.

600 Here it should be highlighted again that the vertical lofting of the volcanic cloud is related to the BDC with an upward branch in the tropics. The patterns in Fig. 5 are a prime example of the stratospheric tape-recorder effect, noticed earlier. For the model experiment, one should bear in mind that the absorption of terrestrial radiation by stratospheric aerosols causes an additional vertical updraft which enhances the BDC effect in the tropics (Niemeier et al., 2011).

4.1 Radiative forcing

605 In order to assess the RF from the Ambae eruption, we analyzed the top-of-the-atmosphere ECHAM RF output as well as the top-of-the-atmosphere RF calculated from OMPS-LP measurements. For the latter, we use the empirical approximation given by Eq. (1) as suggested by Hansen et al. (2005):

$$RF \approx -25 \cdot \tau_{550}, \quad (1)$$

where τ_{550} is the stratospheric aerosol optical depth at 550 nm. Although originally proposed for the globally averaged model data, Eq. (1) was successfully used for the RF assessment from the measurement results as well (see e.g. Solomon et al., 2011; von Savigny et al., 2015). As the focus of our study is on the additional RF after the tropical Ambae eruptions, we do not consider global averages but limit the comparison to 20° S – 20° N region.

To apply Eq. (1) to the OMPS-LP data, we determined $\tau_{550(869)}$ by integrating the Ext_{869} from instantaneous tropopause height to 33.5 km and then converted-converting the result to 550 nm wavelength by using an Ångström exponent of 2.47, which is appropriate for the particle size distribution used in the Ext_{869} retrieval (see Sec. 3.2). The tropopause height values were obtained for each single OMPS-LP measurement by using corresponding ECMWF-ERA5 temperature profiles. The WMO definition of the tropopause based on the temperature lapse rate was implemented (WMO, 1957). Afterwards the $\tau_{550(869)}$ values were averaged over 10-days period. For consistency, we also applied Eq. (1) to the ECHAM τ . Additionally, from all datasets mean tropical τ in the period from 01 April to 19 July 2018 was subtracted to remove the effects of background aerosol. Even though the chosen period contains the effects of the first weaker Ambae eruption, it is a common "cleaner" period available for all datasets and thus is considered to be optimal for the study.

The normalized RFs are presented in Fig. 6. Here, the tropical top-of-the-atmosphere all-sky RF, calculated as an anomaly to a control simulation without the Ambae eruption, is presented with a green line as a function of time. The OMPS-LP RF, calculated employing Eq. (1), is shown with a red line. To illustrate the validity of the Hansen's formula to a non-global dataset, it was also applied to the τ_{550} obtained directly from the ECHAM model. The result is shown with the solid blue line in the figure. The influence of the assumed particle size distribution on the Ext and/or τ conversion to a different wavelength is illustrated by the recalculation of ECHAM τ_{869} to $\tau_{550(869)}$ using the fixed Ångström exponent as it was done for OMPS-LP. The RF resulting from Eq. (1) applied to ECHAM τ_{869} converted to $\tau_{550(869)}$ is presented with a dashed blue line in Fig. 6. Both dates of Ambae eruptions are marked with vertical dotted grey lines.

630 Analyzing the Fig. 6, it becomes obvious that the effect of the first smaller Ambae eruption is negligible for the RF. All four lines show almost no temporal change in between the eruptions (1 April to 27 July 2018) and are located around 0 W/m². Even though from all datasets the RF for the period was subtracted, it was a mean value, resulting in temporal behavior being

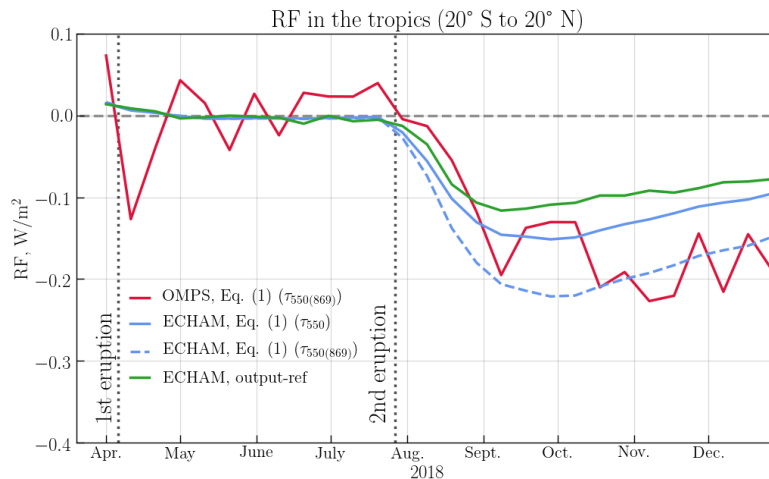


Figure 6. The radiative forcing (RF) from ECHAM and OMPS-LP averaged over the tropics (20° S – 20° N). The green line shows the difference between ECHAM internal RF calculated accounting for and neglecting the Ambae eruptions. Red and blue lines show respectively the RF calculated with Eq. (1) from OMPS-LP τ_{869} converted to $\tau_{550(869)}$, ECHAM τ_{550} (blue solid) and ECHAM τ_{869} converted to $\tau_{550(869)}$ (blue dashed). From all datasets the respective mean RF in the period from the 1 April to the 19 July 2018 was subtracted.

unaffected by this normalization. After the second eruption, all four lines drop significantly. The ECHAM internal RF (green line) reaches its maximum of -0.11 W/m^2 in the first week of September, and afterwards the RF declines slowly up to -0.08 W/m^2 by the late December 2018. The solid blue line, or the RF calculated with Eq. (1) from ECHAM τ_{550} , has very similar behavior with the green line; however, it reaches ~~the~~-its maximum (-0.13 W/m^2) in the late September and keeps the offset from the green line by $\approx 0.02 \text{ W/m}^2$ until the end of 2018. The calculated RF from ECHAM $\tau_{550(869)}$ reaches its maximum at the same time as the solid blue line, but its absolute value is significantly larger (-0.22 W/m^2). Further with time, the offset between ~~the~~ dashed and solid blue lines becomes somewhat smaller, reaching a value of 0.05 W/m^2 in December. At the same time, the red line showing the RF calculated with Eq. 1 from OMPS-LP drops heavily after the second eruption but becomes noisier from September on. The maximum in RF (-0.22 W/m^2) is observed in November 2018 ~~;~~-which agrees ~~with-in agreement with the maximum of the extinction coefficient seen in the panel (a) of Fig. 5.~~ The OMPS-LP RF decreases afterwards to about -0.19 W/m^2 by the end of the year.

In the discussion of Fig. 6, it is important to draw ~~the~~ reader's attention to the offset between the ECHAM RFs calculated with Eq. (1) from τ_{550} and $\tau_{550(869)}$. After the second eruption, the difference reaches up to 70%. This difference is a prime example of the influence of assumed particle size distribution parameters on the RF calculations. For example, at the plume maximum, the difference is almost as large as the forcing, but it decreases while the stratosphere relaxes. ~~Considering-In spite of~~ these discrepancies, the respective similarities of the ECHAM $\tau_{550(869)}$ and OMPS-LP RFs (dashed blue and red lines), as well as ECHAM τ_{550} and ECHAM output (solid blue and green lines), are remarkable. Here it should be noted that although

650 there are obvious differences between the curves, they generally have quite good temporal correlation and capture the second eruption very well.

Combining the above mentioned facts, the following ~~conclusion~~ conclusions can be drawn. Even when applied to the tropical region rather than globally, ~~the~~ Hansen's formula given by Eq. (1) provides a reliable approximation of RF with about 20% accuracy. In turn, the τ conversion to a different wavelength is a more significant source of uncertainty with a potential to
655 increase the estimated RF by up to 70%. After accounting for those uncertainties, a very good agreement between the RF values from ECHAM and those from OMPS-LP is observed. For the particular Ambae eruption studied in this paper, [using Hansen's formula](#), we estimate the tropical ~~radiative forcing~~ RF caused by an increase in stratospheric aerosols to be about -0.13 W/m^2 .

The value obtained for the Ambae RF in this study is significantly lower than that reported by Kloss et al. (2020). In our
660 opinion, the main reason for the disagreement is the way of subtraction of the non-Ambae signal. By subtracting the radiative forcing just before the second eruption we ensure that only the Ambae contribution is accounted for. On the contrary, Kloss et al. (2020) use some "background aerosol" scenario, which is not clearly described in their paper, to remove other contributions than that of Ambae. Another issue can be related to the definition of the tropopause. Although it is not stated clearly, from the remark "(full profiles, for the whole stratosphere)" in Kloss et al. (2020), we guess that only stratospheric part
665 of the aerosol profile is used to calculate the radiative forcing, i.e. the same approach as that in our study is used. If our guess is wrong and Kloss et al. (2020) use tropospheric part of the profiles as well, this might be a reason for the observed disagreement. Otherwise, there might still be a difference in the definition of the tropopause and thus in the calculation of the lowermost altitude in the stratosphere. Kloss et al. (2020) do not provide the definition of the tropopause they use which complicates a direct comparison. There are also some general issues associated with the calculation of small differences of two large values
670 (i.e. radiative forcing from the fluxes) when using a radiative transfer model. These are related to adequate gridding (altitude, streams, Fourier terms, solar zenith angles), the possible need to account for the atmospheric sphericity for the scattered light (i.e. going beyond the pseudo-spherical solution), and possible implications of using a simple parametrization of the aerosol scattering with an asymmetry parameter.

5 Conclusions

675 The distribution of aerosol extinction coefficients at 869 nm in the stratosphere after the 2018 Ambae eruption was compared using the data retrieved from the OMPS-LP observations and that modeled by ECHAM.

We present here the retrieval algorithm (V1.0.9) of stratospheric aerosol extinction coefficient profiles at 869 nm from the OMPS-LP instrument. The retrieval algorithm was adopted from SCIAMACHY V1.4 and shows similar results in comparison with solar occultation instruments. The comparison of [the](#) OMPS V1.0.9 product with the aerosol extinction coefficient obser-
680 vations from SAGE III/ISS showed that the mean relative difference is less than 25% for the profiles in between 40° S and 40° N. In the higher latitudes, the difference is somewhat larger; it is less than 35% below 25 km but can reach about 60% at 28 km.

We also show the changes in the aerosol extinction coefficient after the 2018 Ambae eruption using monthly mean and 10-day average data. Ambae caused one of the largest perturbations in the aerosol layer for the OMPS operating period. Volcanic aerosols rise over time to about 21 km in the tropics within the tropical pipe of BDC (the tape-recorder effect). Analysing the 10-day average data, it has been ~~seen-observed~~ that the plume from the first phase of the eruption was relatively weak and did not spread outside ~~the~~ tropics. The second eruption in July was much larger, and the aerosols also spread to the mid-latitudes of both hemispheres.

The measurement data was compared with the model output from a ~~global-aerosol-model~~ GCM with coupled aerosol microphysics (ECHAM). In order to simulate the Ambae eruption accurately, the injected SO₂ emission was estimated using combined OMPS and OMI data for the April eruption (0.12 Tg) and TROPOMI data for the July eruption (≈ 0.36 Tg). The altitudinal distribution of the SO₂ was assessed using MLS profiles. Thus, the resulting simulation showed that the model and measurements agree well with each other. The main differences concern the intensity and the lifetime of the volcanic perturbation. ~~While-for~~ For the first eruption, ECHAM underestimated the strength of ~~the~~ plume as well as the time ~~it-reached-by~~ which it reaches 20.5 ~~km-altitude;~~ km of altitude, whereas for the second eruption, the modeled plume reached higher altitudes about two to three weeks earlier, and the plume lived longer, ~~being-overall-slightly-weaker-at-that-altitude~~ while being slightly weaker overall at those altitudes. Although the differences ~~in-between~~ the measured and modeled plumes exist, they are rather minor, and the consistency is remarkable. The good agreement is explained by the rather precise SO₂ injection mass and height assessment, as well as by the nudging of meteorological data.

We also compare ~~aerosol-the top-of-the-atmosphere~~ radiative forcing (RF) ~~in the tropics~~ caused by the increase in stratospheric aerosol loading from the second Ambae eruption ~~in the tropics~~. While the time ~~courses-of-RF-for evolution of RF from~~ the ECHAM output and ECHAM and OMPS-LP ~~re-calculated-RFs-stratospheric aerosol optical depths~~ generally agree quite well, the absolute values vary significantly. The empirical formula used in our assessment works well not only for the globally averaged aerosol optical depths but also for the tropical region. However, this approach suffers from the errors associated with the assumed particle size distribution for the datasets where the ~~Ångström-ngström~~ exponent has to be used ~~to convert stratospheric optical depth to another wavelength~~. We estimate the RF in the tropics after the second 2018 Ambae eruption to be about -0.13 W/m².

In general, if the initial data (SO₂ mass, day and height of injection as well as meteorological data) is quite precise, the ~~models-give-model~~ gives a very good estimate of the plume distribution, and the calculation of the radiative forcing can be made for an isolated plume without additional assumptions. Overall, the best results can be achieved only by combining observational data and modeling capabilities. Thus, it is very important to unite the measurement and model community together, for example, as the research unit VolImpact does (von Savigny et al., 2020).

Appendix A: Estimation of SO₂ injection height

As it was pointed out in Sec. 3.1, in order to find out SO₂ injection heights, we used MLS (Sec. 2.4) SO₂ number density profiles. Using the plume locations from the nadir instruments, OMI/OMPS-NM for April eruption and TROPOMI for July

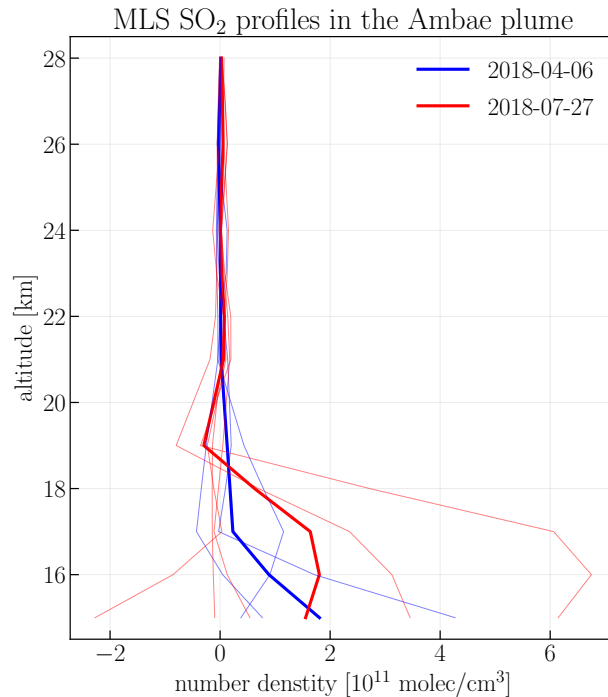


Figure A1. MLS SO₂ number density profiles in the Ambae plume on the 6th April (blue lines) and on the 27th of July (red lines) 2018. The thick lines show mean profile, while thin lines depict individual measurements within the plume.

eruption, we determined the days when the SO₂ reached UTLS. We show these profiles in Fig. A1. For the first eruption, which happened on the 6 April 2018, the profiles are depicted in blue, while the profiles for the second eruption on the 27 July 2018 are red. The individual profiles in the plume are plotted with thin lines, while the average profile for the area are shown by the thicker line. On the 6 April, the SO₂ cloud was located in between 15 and 17 km. The tropopause height, according to the MLS data, was in between 16.7 to 17.5 km for the Ambae plume location. For the 27 July, the SO₂ cloud was detected in between 15 and about 18 km, while the tropopause height was located between 15.9 and 16.5 km. We used this information to simulate the Ambae eruption with ECHAM, the results are presented in Sec. 4.0.1.

Appendix B: Impact of the assumed SO₂ profile on the SO₂ mass estimate

The estimate of the ejected SO₂ mass during the Ambae eruption depends strongly on the assumed SO₂ profile. TROPOMI satellite data provides the total sulfur dioxide vertical column densities for three different box profiles that assume an SO₂ filled 1 km thick box centered on ground level, in 7 km and in 15 km altitude above sea level, respectively. To illustrate the importance of the profile choice, the SO₂ mass for the 2018 July Ambae eruption was calculated using TROPOMI data that either assumes an SO₂ box profile at 7 km or 15 km altitude above sea level. A threshold of 0.05 g/m² was applied and the results were

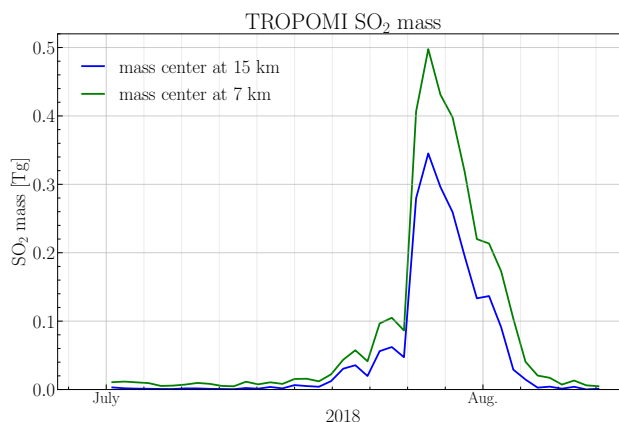


Figure B1. SO₂ mass from TROPOMI for the 7 km (green line) and the 15 km (blue line) SO₂ profile.

730 presented in Figure B1, where the blue line shows the estimates for 15 km profile and the green line depicts the estimates for 7 km profile. The calculated SO₂ mass clearly differ with the maximum value of 0.35 Tg for the 15 km box profile being smaller than the estimate of 0.5 Tg for the 7 km box profile.

Code and data availability. OMPS-LP aerosol extinction coefficient at 869 nm data are available after registration at <http://www.iup.uni-bremen.de/DataRequest/>. ECHAM primary data and scripts used in the analysis and other supplementary information that may be useful in reproducing the authors model work are archived by the Max Planck Institute for Meteorology and can be obtained by contacting publicat-
735 tions@mpimet.mpg.de. Model results will be available under cera-www.dkrz.de soon.

Author contributions. EM initiated the study, provided OMPS-LP aerosol extinction coefficient product, compared it to SAGE-III/ISS, prepared the Figures and wrote most of the paper text (Sec. 1 - 2.6, 3.2 - 5). AR developed the retrieval software, supervised the work at the University of Bremen, wrote part of Sec. 4.1 and revised the rest paper. UN performed model simulations, wrote Sec. 2.7, and 4.0.1, helped with the literature survey and revised the text. SW performed SO₂ mass estimations, wrote Sec. 3.1, provided data for Figs. 1 and B1 and
740 revised the text. CA formatted OMPS L1 data, analyzed MLS data, provided data for Fig. A1 and tropopause heights for OMPS-LP as well as revised the text. FW actively participated in the result discussions and revised the text. CT helped with literature survey; CvS and CT initiated and proposed the research unit, they and JPB led the project and revised the text.

Competing interests. The authors declare no competing interests.

Acknowledgements. This work was funded in parts by the German Research Foundation (DFG) through the research unit VolImpact (FOR 745 2820): projects VolARC, VolDyn and VolClim, ESA through Ozone-CCI+ project, and the University of Bremen and state of Bremen. The model simulations were performed on the computer of the Deutsches Klima Rechenzentrum (DKRZ). We are also thankful to NASA for OMI (NASA GES DISC, 2020a) and OMPS-NM (NASA GES DISC, 2020b) L2 data as well as for OMPS-LP L1 data which was downloaded from the NASA Langley Research Center EOSDIS Distributed Active Archive Center. MLS and SAGE-III/ISS L2 data was obtained from NASA's Earthdata (2020a) and NASA's Earthdata (2020b) respectively. S5P TROPOMI data was downloaded from S5P Data Hub (2020).

750 References

- Arosio, C., Rozanov, A., Malinina, E., Eichmann, K.-U., von Clarmann, T., and Burrows, J. P.: Retrieval of ozone profiles from OMPS limb scattering observations, *Atmospheric Measurement Techniques*, 11, 2135–2149, <https://doi.org/10.5194/amt-11-2135-2018>, <https://www.atmos-meas-tech.net/11/2135/2018/>, 2018.
- Bertaux, J., Hauchecorne, A., Dalaudier, F., Cot, C., Kyrölä, E., Fussen, D., Tamminen, J., Leppelmeier, G., Sofieva, V., Hassinen, S., et al.: First results on GOMOS/Envisat, *Advances in Space Research*, 33, 1029–1035, 2004.
- Bingen, C., Fussen, D., and Vanhellemont, F.: A global climatology of stratospheric aerosol size distribution parameters derived from SAGE II data over the period 1984–2000: 1. Methodology and climatological observations, *Journal of Geophysical Research: Atmospheres*, 109, 2004.
- Bourassa, A. E., Rieger, L. A., Zawada, D. J., Khaykin, S., Thomason, L., and Degenstein, D. A.: Satellite Limb Observations of Unprecedented Forest Fire Aerosol in the Stratosphere, *Journal of Geophysical Research: Atmospheres*, <https://doi.org/10.1029/2019JD030607>, 2019.
- Brinkhoff, L. A., Rozanov, A., Hommel, R., von Savigny, C., Ernst, F., Bovensmann, H., and Burrows, J. P.: Ten-Year SCIAMACHY Stratospheric Aerosol Data Record: Signature of the Secondary Meridional Circulation Associated with the Quasi-Biennial Oscillation, in: *Towards an Interdisciplinary Approach in Earth System Science*, pp. 49–58, Springer, 2015.
- Brühl, C., Schalllock, J., Klingmüller, K., Robert, C., Bingen, C., Clarisse, L., Heckel, A., North, P., and Rieger, L.: Stratospheric aerosol radiative forcing simulated by the chemistry climate model EMAC using Aerosol CCI satellite data, *Atmospheric Chemistry and Physics*, 18, 12 845–12 857, <https://doi.org/10.5194/acp-18-12845-2018>, <https://www.atmos-chem-phys.net/18/12845/2018/>, 2018.
- Carboni, E., Grainger, R. G., Mather, T. A., Pyle, D. M., Thomas, G. E., Siddans, R., Smith, A. J. A., Dudhia, A., Koukouli, M. E., and Balis, D.: The vertical distribution of volcanic SO₂ plumes measured by IASI, *Atmospheric Chemistry and Physics*, 16, 4343–4367, <https://doi.org/10.5194/acp-16-4343-2016>, <https://www.atmos-chem-phys.net/16/4343/2016/>, 2016.
- Carn, S., Yang, K., Prata, A., and Krotkov, N.: Extending the long-term record of volcanic SO₂ emissions with the Ozone Mapping and Profiler Suite nadir mapper, *Geophysical Research Letters*, 42, 925–932, 2015.
- Chen, Z., DeLand, M., and Bhartia, P. K.: A new algorithm for detecting cloud height using OMPS/LP measurements, *Atmospheric Measurement Techniques*, 9, 1239–1246, <https://doi.org/10.5194/amt-9-1239-2016>, <https://amt.copernicus.org/articles/9/1239/2016/>, 2016.
- Chen, Z., Bhartia, P. K., Loughman, R., Colarco, P., and DeLand, M.: Improvement of stratospheric aerosol extinction retrieval from OMPS/LP using a new aerosol model, *Atmospheric Measurement Techniques*, 11, 6495–6509, <https://doi.org/10.5194/amt-11-6495-2018>, <https://www.atmos-meas-tech.net/11/6495/2018/>, 2018.
- Chen, Z., Bhartia, P. K., Torres, O., Jaross, G., Loughman, R., DeLand, M., Colarco, P., Damadeo, R., and Taha, G.: Evaluation of OMPS/LP Stratospheric Aerosol Extinction Product Using SAGE III/ISS Observations, *Atmospheric Measurement Techniques Discussions*, 2019, 1–27, <https://doi.org/10.5194/amt-2019-360>, <https://www.atmos-meas-tech-discuss.net/amt-2019-360/>, 2019.
- Cisewski, M., Zawodny, J., Gasbarre, J., Eckman, R., Topiwala, N., Rodriguez-Alvarez, O., Cheek, D., and Hall, S.: The Stratospheric Aerosol and Gas Experiment (SAGE III) on the International Space Station (ISS) Mission, in: *Sensors, Systems, and Next-Generation Satellites XVIII*, vol. 9241, p. 924107, International Society for Optics and Photonics, 2014.
- Clyne, M., Lamarque, J.-F., Mills, M. J., Khodri, M., Ball, W., Bekki, S., Dhomse, S. S., Lebas, N., Mann, G., Marshall, L., Niemeier, U., Poulain, V., Robock, A., Rozanov, E., Schmidt, A., Stenke, A., Sukhodolov, T., Timmreck, C., Toohey, M., Tummon, F., Zanchettin, D., Zhu, Y., and Toon, O. B.: Model physics and chemistry causing intermodel disagreement within the VolMIP-Tambora Interactive

- Stratospheric Aerosol ensemble, *Atmospheric Chemistry and Physics*, 21, 3317–3343, <https://doi.org/10.5194/acp-21-3317-2021>, <https://acp.copernicus.org/articles/21/3317/2021/>, 2021.
- 790 Damadeo, R., Zawodny, J., Thomason, L., and Iyer, N.: SAGE version 7.0 algorithm: application to SAGE II, *Atmospheric Measurement Techniques*, 6, 3539–3561, 2013.
- Dhomse, S. S., Mann, G. W., Antuña Marrero, J. C., Shallcross, S. E., Chipperfield, M. P., Carslaw, K. S., Marshall, L., Abraham, N. L., and Johnson, C. E.: Evaluating the simulated radiative forcings, aerosol properties and stratospheric warmings from the 1963 Agung, 1982 El Chichón and 1991 Mt Pinatubo volcanic aerosol clouds, *Atmospheric Chemistry and Physics Discussions*, 2020, 1–45, <https://doi.org/10.5194/acp-2020-344>, <https://www.atmos-chem-phys-discuss.net/acp-2020-344/>, 2020.
- 795 Feinberg, A., Sukhodolov, T., Luo, B.-P., Rozanov, E., Winkel, L. H., Peter, T., and Stenke, A.: Improved tropospheric and stratospheric sulfur cycle in the aerosol-chemistry-climate model SOCOL-AERv2, *Geoscientific Model Development*, 12, 3863–3887, 2019.
- Fioletov, V., McLinden, C., Krotkov, N., Moran, M., and Yang, K.: Estimation of SO₂ emissions using OMI retrievals, *Geophysical Research Letters*, 38, 2011.
- Fioletov, V., McLinden, C. A., Griffin, D., Theys, N., Loyola, D. G., Hedelt, P., Krotkov, N. A., and Li, C.: Anthropogenic and volcanic point source SO₂ emissions derived from TROPOMI onboard Sentinel 5 Precursor: first results, *Atmospheric Chemistry and Physics Discussions*, 2020, 1–30, <https://doi.org/10.5194/acp-2019-1095>, <https://www.atmos-chem-phys-discuss.net/acp-2019-1095/>, 2020.
- 800 Fioletov, V. E., McLinden, C. A., Krotkov, N., Li, C., Joiner, J., Theys, N., Carn, S., and Moran, M. D.: A global catalogue of large SO₂ sources and emissions derived from the Ozone Monitoring Instrument, *Atmospheric Chemistry and Physics*, 16, 11 497–11 519, 2016.
- Fischer, H., Birk, M., Blom, C., Carli, B., Carlotti, M., Clarmann, T. v., Delbouille, L., Dudhia, A., Ehhalt, D., Endemann, M., et al.: MIPAS: an instrument for atmospheric and climate research, *Atmospheric Chemistry and Physics*, 8, 2151–2188, 2008.
- 805 Flynn, L., Long, C., Wu, X., Evans, R., Beck, C., Petropavlovskikh, I., McConville, G., Yu, W., Zhang, Z., Niu, J., et al.: Performance of the ozone mapping and profiler suite (OMPS) products, *Journal of Geophysical Research: Atmospheres*, 119, 6181–6195, 2014.
- Fromm, M., Lindsey, D. T., Servranckx, R., Yue, G., Trickl, T., Sica, R., Doucet, P., and Godin-Beekmann, S.: The untold story of pyrocumulonimbus, *Bulletin of the American Meteorological Society*, 91, 1193–1210, 2010.
- 810 Fussen, D. and Bingen, C.: Volcanism dependent model for the extinction profile of stratospheric aerosols in the UV-visible range, *Geophysical research letters*, 26, 703–706, 1999.
- Giorgetta, M. A., Manzini, E., Roeckner, E., Esch, M., and Bengtsson, L.: Climatology and forcing of the quasi-biennial oscillation in the MAECHAM5 model, *J. Climate*, 19, 3882–3901, 2006.
- Gottwald, M. and Bovensmann, H.: *SCIAMACHY - Exploring the Changing Earth's Atmosphere*, Springer, Dordrecht, <https://doi.org/10.1007/978-90-481-9896-2>, 2011.
- 815 Hansen, J., Sato, M., Ruedy, R., Nazarenko, L., Lacis, A., Schmidt, G., Russell, G., Aleinov, I., Bauer, M., Bauer, S., et al.: Efficacy of climate forcings, *Journal of Geophysical Research: Atmospheres*, 110, 2005.
- Haywood, J. M., Jones, A., Clarisse, L., Bourassa, A., Barnes, J., Telford, P., Bellouin, N., Boucher, O., Agnew, P., Clerbaux, C., et al.: Observations of the eruption of the Sarychev volcano and simulations using the HadGEM2 climate model, *Journal of Geophysical Research: Atmospheres*, 115, 2010.
- 820 Haywood, J. M., Jones, A., and Jones, G. S.: The impact of volcanic eruptions in the period 2000–2013 on global mean temperature trends evaluated in the HadGEM2-ES climate model, *Atmospheric Science Letters*, 15, 92–96, 2014.

- Hersbach, H., de Rosnay, P., Bell, B., Schepers, D., Simmons, A., Soci, C., Abdalla, S., Alonso-Balmaseda, M., Balsamo, G., Bechtold, P., et al.: Operational global reanalysis: progress, future directions and synergies with NWP, ERA Report Series, ECMWF, Shinfield Park, 825 2018.
- Hess, M., Koepke, P., and Schult, I.: Optical properties of aerosols and clouds: The software package OPAC, *Bulletin of the American meteorological society*, 79, 831–844, 1998.
- Hitchman, M. H., McKay, M., and Trepte, C. R.: A climatology of stratospheric aerosol, *Journal of Geophysical Research: Atmospheres*, 99, 20 689–20 700, 1994.
- 830 Hommel, R., Timmreck, C., and Graf, H. F.: The global middle-atmosphere aerosol model MAECHAM5-SAM2: comparison with satellite and in-situ observations, *Geoscientific Model Development*, 4, 809–834, <https://doi.org/10.5194/gmd-4-809-2011>, <http://www.geosci-model-dev.net/4/809/2011/>, 2011.
- Hommel, R., Timmreck, C., Giorgetta, M. A., and Graf, H. F.: Quasi-biennial oscillation of the tropical stratospheric aerosol layer, *Atmospheric Chemistry and Physics*, 15, 5557–5584, <https://doi.org/10.5194/acp-15-5557-2015>, <https://www.atmos-chem-phys.net/15/5557/> 835 2015/, 2015.
- Hurrell, J. W., Hack, J. J., Shea, D., Caron, J. M., and Rosinski, J.: A New Sea Surface Temperature and Sea Ice Boundary Dataset for the Community Atmosphere Model, *Journal of Climate*, 21, 5145–5153, <https://doi.org/10.1175/2008JCLI2292.1>, <https://doi.org/10.1175/2008JCLI2292.1>, 2008.
- Ivy, D. J., Solomon, S., Kinnison, D., Mills, M. J., Schmidt, A., and Neely, R. R.: The influence of the Calbuco eruption on the 2015 Antarctic 840 ozone hole in a fully coupled chemistry-climate model, *Geophysical Research Letters*, 44, 2556–2561, 2017.
- Jaross, G., Bhartia, P. K., Chen, G., Kowitt, M., Haken, M., Chen, Z., Xu, P., Warner, J., and Kelly, T.: OMPS Limb Profiler instrument performance assessment, *Journal of Geophysical Research: Atmospheres*, 119, 4399–4412, <https://doi.org/10.1002/2013JD020482>, <http://dx.doi.org/10.1002/2013JD020482>, 2014.
- Kang, M.-J. and Chun, H.-Y.: Contributions of equatorial planetary waves and small-scale convective gravity waves to the 2019/20 QBO 845 disruption, *Atmospheric Chemistry and Physics Discussions*, 2021, 1–33, <https://doi.org/10.5194/acp-2021-85>, <https://acp.copernicus.org/preprints/acp-2021-85/>, 2021.
- Khaykin, S., Godin-Beekmann, S., Hauchecorne, A., Pelon, J., Ravetta, F., and Keckhut, P.: Stratospheric smoke with unprecedentedly high backscatter observed by lidars above southern France, *Geophysical Research Letters*, 45, 1639–1646, 2018.
- Khaykin, S., Legras, B., Bucci, S., Sellitto, P., Isaksen, L., Tence, F., Bekki, S., Bourassa, A., Rieger, L., Zawada, D., Jumelet, J., and Godin- 850 Beekmann, S.: The 2019/20 Australian wildfires generated a persistent smoke-charged vortex rising up to 35 km altitude, *Communications Earth & Environment*, 1, 1–12, 2020.
- Kloss, C., Berthet, G., Sellitto, P., Ploeger, F., Bucci, S., Khaykin, S., Jégou, F., Taha, G., Thomason, L. W., Barret, B., Le Flochmoen, E., von Hobe, M., Bossolasco, A., Bègue, N., and Legras, B.: Transport of the 2017 Canadian wildfire plume to the tropics via the Asian monsoon circulation, *Atmospheric Chemistry and Physics*, 19, 13 547–13 567, <https://doi.org/10.5194/acp-19-13547-2019>, <https://www.atmos-chem-phys.net/19/13547/2019/>, 2019. 855
- Kloss, C., Sellitto, P., Legras, B., Vernier, J.-P., Jégou, F., Venkat Ratnam, M., Kumar, B. S., Madhavan, B. L., and Berthet, G.: Impact of the 2018 Ambae eruption on the global stratospheric aerosol layer and climate, *Journal of Geophysical Research: Atmospheres*, p. e2020JD032410, 2020.
- Kravitz, B., Robock, A., and Bourassa, A.: Negligible climatic effects from the 2008 Okmok and Kasatochi volcanic eruptions, *Journal of* 860 *Geophysical Research: Atmospheres*, 115, 2010.

- Kravitz, B., Robock, A., Bourassa, A., Deshler, T., Wu, D., Mattis, I., Finger, F., Hoffmann, A., Ritter, C., Bitar, L., et al.: Simulation and observations of stratospheric aerosols from the 2009 Sarychev volcanic eruption, *Journal of Geophysical Research: Atmospheres*, 116, 2011.
- 865 Kremser, S., Thomason, L. W., Hobe, M., Hermann, M., Deshler, T., Timmreck, C., Toohey, M., Stenke, A., Schwarz, J. P., Weigel, R., et al.: Stratospheric aerosol—Observations, processes, and impact on climate, *Reviews of Geophysics*, 2016.
- Levelt, P., van den Oord, G., Dobber, M., Malkki, A., Visser, H., de Vries, J., Stammes, P., Lundell, J., and Saari, H.: The ozone monitoring instrument, *IEEE Transactions on Geoscience and Remote Sensing*, 44, 1093–1101, <https://doi.org/10.1109/TGRS.2006.872333>, 2006.
- Levelt, P. F., Joiner, J., Tamminen, J., Veefkind, J. P., Bhartia, P. K., Stein Zweers, D. C., Duncan, B. N., Streets, D. G., Eskes, H., van der A, R., McLinden, C., Fioletov, V., Carn, S., de Laat, J., DeLand, M., Marchenko, S., McPeters, R., Ziemke, J., Fu, D., Liu, X., Pickering, 870 K., Apituley, A., González Abad, G., Arola, A., Boersma, F., Chan Miller, C., Chance, K., de Graaf, M., Hakkarainen, J., Hassinen, S., Ialongo, I., Kleipool, Q., Krotkov, N., Li, C., Lamsal, L., Newman, P., Nowlan, C., Suleiman, R., Tilstra, L. G., Torres, O., Wang, H., and Wargan, K.: The Ozone Monitoring Instrument: overview of 14 years in space, *Atmospheric Chemistry and Physics*, 18, 5699–5745, <https://doi.org/10.5194/acp-18-5699-2018>, <https://acp.copernicus.org/articles/18/5699/2018/>, 2018.
- Li, C., Krotkov, N. A., Carn, S., Zhang, Y., Spurr, R. J. D., and Joiner, J.: New-generation NASA Aura Ozone Monitoring Instrument (OMI) 875 volcanic SO₂ dataset: algorithm description, initial results, and continuation with the Suomi-NPP Ozone Mapping and Profiler Suite (OMPS), *Atmospheric Measurement Techniques*, 10, 445–458, <https://doi.org/10.5194/amt-10-445-2017>, <https://www.atmos-meas-tech.net/10/445/2017/>, 2017.
- Llewellyn, E., Lloyd, N., Degenstein, D., Gattinger, R., Petelina, S., Bourassa, A., Wiensz, J., Ivanov, E., McDade, I., Solheim, B., et al.: The OSIRIS instrument on the Odin spacecraft, *Canadian Journal of Physics*, 82, 411–422, 2004.
- 880 Loughman, R., Bhartia, P. K., Chen, Z., Xu, P., Nyaku, E., and Taha, G.: The Ozone Mapping and Profiler Suite (OMPS) Limb Profiler (LP) Version 1 aerosol extinction retrieval algorithm: theoretical basis, *Atmospheric Measurement Techniques*, 11, 2633–2651, <https://doi.org/10.5194/amt-11-2633-2018>, <https://www.atmos-meas-tech.net/11/2633/2018/>, 2018.
- Lu, Z., Streets, D. G., de Foy, B., and Krotkov, N. A.: Ozone monitoring instrument observations of interannual increases in SO₂ emissions from Indian coal-fired power plants during 2005–2012, *Environmental science & technology*, 47, 13 993–14 000, 885 <https://doi.org/10.1021/es4039648>, <https://doi.org/10.1021/es4039648>, 2013.
- Lurton, T., Jégou, F., Berthet, G., Renard, J.-B., Clarisse, L., Schmidt, A., Brogniez, C., and Roberts, T. J.: Model simulations of the chemical and aerosol microphysical evolution of the Sarychev Peak 2009 eruption cloud compared to in situ and satellite observations, *Atmospheric Chemistry and Physics*, 18, 3223–3247, <https://doi.org/10.5194/acp-18-3223-2018>, <https://www.atmos-chem-phys.net/18/3223/2018/>, 2018.
- 890 Malinina, E.: Retrieval of stratospheric aerosol characteristics from spaceborne limb sounders, PhD Thesis, University of Bremen, <http://nbn-resolving.de/urn:nbn:de:gbv:46-00107153-12>, 2019.
- Malinina, E., Rozanov, A., Rozanov, V., Liebing, P., Bovensmann, H., and Burrows, J. P.: Aerosol particle size distribution in the stratosphere retrieved from SCIAMACHY limb measurements, *Atmospheric Measurement Techniques*, 11, 2085–2100, <https://doi.org/10.5194/amt-11-2085-2018>, <https://www.atmos-meas-tech.net/11/2085/2018/>, 2018.
- 895 Marshall, L., Schmidt, A., Toohey, M., Carslaw, K. S., Mann, G. W., Sigl, M., Khodri, M., Timmreck, C., Zanchettin, D., Ball, W. T., et al.: Multi-model comparison of the volcanic sulfate deposition from the 1815 eruption of Mt. Tambora, *Atmospheric Chemistry and Physics*, 18, 2307–2328, 2018.

- McCormick, M. P., Lei, L., and Hill, M. T.: Early results and Validation of SAGE III-ISS Ozone Profile Measurements from Onboard the International Space Station, *Atmospheric Measurement Techniques Discussions*, 2019, 1–14, <https://doi.org/10.5194/amt-2019-353>,
900 <https://www.atmos-meas-tech-discuss.net/amt-2019-353/>, 2019.
- Mettig, N., Weber, M., Rozanov, A., Arosio, C., Burrows, J. P., Veefkind, P., Thompson, A. M., Querel, R., Leblanc, T., Godin-Beekmann, S., Kivi, R., and Tully, M. B.: Ozone Profile Retrieval from nadir TROPOMI measurements in the UV range, *Atmospheric Measurement Techniques Discussions*, 2021, 1–36, <https://doi.org/10.5194/amt-2021-32>, <https://amt.copernicus.org/preprints/amt-2021-32/>, 2021.
- Mills, M. J., Richter, J. H., Tilmes, S., Kravitz, B., MacMartin, D. G., Glanville, A. A., Tribbia, J. J., Lamarque, J.-F., Vitt, F., Schmidt, A., Gettelman, A., Hannay, C., Bacmeister, J. T., and Kinnison, D. E.: Radiative and Chemical Response to Interactive Stratospheric Sulfate Aerosols in Fully Coupled CESM1(WACCM), *Journal of Geophysical Research: Atmospheres*, 122, 13,061–13,078,
905 <https://doi.org/10.1002/2017JD027006>, <http://dx.doi.org/10.1002/2017JD027006>, 2017JD027006, 2017.
- Moussallam, Y., Rose-Koga, E. F., Koga, K. T., Médard, E., Bani, P., Devidal, J.-L., and Tari, D.: Fast ascent rate during the 2017–2018 Plinian eruption of Ambae (Aoba) volcano: a petrological investigation, *Contributions to Mineralogy and Petrology*, 174, 90, 2019.
- 910 NASA GES DISC: OMSO2: OMI/Aura Sulphur Dioxide (SO₂) Total Column 1-orbit L2 Swath 13x24 km V003, https://disc.gsfc.nasa.gov/datasets/OMSO2_003/summary, 2020a.
- NASA GES DISC: OMPS_NPP_NMSO2_L2: OMPS-NPP L2 NM Sulfur Dioxide (SO₂) Total and Tropospheric Column swath orbital V2, https://disc.gsfc.nasa.gov/datasets/OMPS_NPP_NMSO2_L2_2/summary, 2020b.
- NASA GES DISC: OMPS_NPP_Products, <https://disc.gsfc.nasa.gov/datasets?keywords=omps&page=1&source=SUOMI-NPP%20OMPS>,
915 2021.
- NASA's Earthdata: MLS/Aura Level 2 Sulfur Dioxide (SO₂) Mixing Ratio V004 (ML2SO₂) at GES DISC, https://search.earthdata.nasa.gov/search?p=C1251101777-GES_DISC&q=ML2SO2_004, 2020a.
- NASA's Earthdata: SAGE III/ISS L2 Solar Event Species Profiles (HDF-EOS) V051, [https://search.earthdata.nasa.gov/search/granules?p=C1576312558-LARC&fpj=SAGE%20III/ISS&as\[project\]\[0\]=SAGE%20III/ISS&tl=1574370747!4!!](https://search.earthdata.nasa.gov/search/granules?p=C1576312558-LARC&fpj=SAGE%20III/ISS&as[project][0]=SAGE%20III/ISS&tl=1574370747!4!!), 2020b.
- 920 Newman, P., Coy, L., Pawson, S., and Lait, L.: The anomalous change in the QBO in 2015–2016, *Geophysical Research Letters*, 43, 8791–8797, 2016.
- Niemeier, U. and Timmreck, C.: What is the limit of climate engineering by stratospheric injection of SO₂?, *Atmospheric Chemistry and Physics*, 15, 9129–9141, <https://doi.org/10.5194/acp-15-9129-2015>, <http://www.atmos-chem-phys.net/15/9129/2015/>, 2015.
- Niemeier, U., Timmreck, C., Graf, H.-F., Kinne, S., Rast, S., and Self, S.: Initial fate of fine ash and sulfur from large volcanic eruptions, *Atmospheric Chemistry and Physics*, 9, 9043–9057, <http://www.atmos-chem-phys.net/9/9043/2009/>, 2009.
- 925 Niemeier, U., Schmidt, H., and Timmreck, C.: The dependency of geoengineered sulfate aerosol on the emission strategy, *Atmospheric Science Letters*, 12, 189–194, 2011.
- Oman, L., Robock, A., Stenchikov, G. L., Thordarson, T., Koch, D., Shindell, D. T., and Gao, C.: Modeling the distribution of the volcanic aerosol cloud from the 1783–1784 Laki eruption, *Journal of Geophysical Research: Atmospheres*, 111, 2006.
- 930 Pedergnana, M., Loyola, D., Apituley, A., Sneep, M., and Veefkind, J. P.: Sentinel-5 precursor/TROPOMI Level 2 Product User Manual Sulphur Dioxide SO₂, 2018.
- Pitari, G., Visioni, D., Mancini, E., Cionni, I., Di Genova, G., and Gandolfi, I.: Sulfate aerosols from non-explosive volcanoes: chemical-radiative effects in the troposphere and lower stratosphere, *Atmosphere*, 7, 85, 2016.
- Pumphrey, H. C., Read, W. G., Livesey, N. J., and Yang, K.: Observations of volcanic SO₂ from MLS on Aura, *Atmospheric Measurement Techniques*, 8, 195–209, <https://doi.org/10.5194/amt-8-195-2015>, <https://www.atmos-meas-tech.net/8/195/2015/>, 2015.
- 935

- Randel, W. J., Park, M., Emmons, L., Kinnison, D., Bernath, P., Walker, K. A., Boone, C., and Pumphrey, H.: Asian monsoon transport of pollution to the stratosphere, *Science*, 328, 611–613, 2010.
- Rieger, L., Zawada, D., Bourassa, A., and Degenstein, D.: A multiwavelength retrieval approach for improved OSIRIS aerosol extinction retrievals, *Journal of Geophysical Research: Atmospheres*, 124, 7286–7307, 2019.
- 940 Rieger, L. A., Malinina, E. P., Rozanov, A. V., Burrows, J. P., Bourassa, A. E., and Degenstein, D. A.: A study of the approaches used to retrieve aerosol extinction, as applied to limb observations made by OSIRIS and SCIAMACHY, *Atmospheric Measurement Techniques Discussions*, 2018, 1–21, <https://doi.org/10.5194/amt-2017-446>, <https://www.atmos-meas-tech-discuss.net/amt-2017-446/>, 2018.
- S5P Data Hub: Sentinel-P Pre-Operations Data Hub, <https://s5phub.copernicus.eu/dhus/#/home>, 2020.
- Schmidt, A., Mills, M. J., Ghan, S., Gregory, J. M., Allan, R. P., Andrews, T., Bardeen, C. G., Conley, A., Forster, P. M., Gettelman, A., et al.:
- 945 Volcanic radiative forcing from 1979 to 2015, *Journal of Geophysical Research: Atmospheres*, 123, 12 491–12 508, 2018.
- Seftor, C., Jaross, G., Kowitt, M., Haken, M., Li, J., and Flynn, L.: Postlaunch performance of the Suomi National Polar-orbiting Partnership Ozone Mapping and Profiler Suite (OMPS) nadir sensors, *Journal of Geophysical Research: Atmospheres*, 119, 4413–4428, 2014.
- Siddaway, J. and Petelina, S.: Transport and evolution of the 2009 Australian Black Saturday bushfire smoke in the lower stratosphere observed by OSIRIS on Odin, *Journal of Geophysical Research: Atmospheres*, 116, 2011.
- 950 Smithsonian Institution: Global Volcanism Program Database, http://volcano.si.edu/search_eruption.cfm, 2019.
- Solomon, S.: Stratospheric ozone depletion: A review of concepts and history, *Reviews of Geophysics*, 37, 275–316, 1999.
- Solomon, S., Daniel, J. S., Neely, R. R., Vernier, J.-P., Dutton, E. G., and Thomason, L. W.: The persistently variable “background” stratospheric aerosol layer and global climate change, *Science*, 333, 866–870, 2011.
- Stier, P., Feichter, J., Kinne, S., Kloster, S., Vignati, E., Wilson, J., Ganzeveld, L., Tegen, I., Werner, M., Balkanski, Y., Schulz, M., Boucher,
- 955 O., Minikin, A., and Petzold, A.: The aerosol–climate model ECHAM5–HAM, *Atmos. Chem. Phys.*, 5, 1125–1156, 2005.
- Theys, N., De Smedt, I., Yu, H., Danckaert, T., van Gent, J., Hörmann, C., Wagner, T., Hedelt, P., Bauer, H., Romahn, F., Pedergnana, M., Loyola, D., and Van Roozendael, M.: Sulfur dioxide retrievals from TROPOMI onboard Sentinel-5 Precursor: algorithm theoretical basis, *Atmospheric Measurement Techniques*, 10, 119–153, <https://doi.org/10.5194/amt-10-119-2017>, <https://www.atmos-meas-tech.net/10/119/2017/>, 2017.
- 960 Theys, N., Romahn, F., and Wagner, T.: S5P Mission Performance Centre Sulphur Dioxide Readme, <https://sentinel.esa.int/documents/247904/3541451/Sentinel-5P-Sulphur-Dioxide-Readme.pdf>, s5P-MPC-BIRA-PRF-SO2, V02.01.04, 2020.
- Thomason, L. and Peter, T.: SPARC Assessment of Stratospheric Aerosol Properties (ASAP), Tech. rep., SPARC, <http://www.sparc-climate.org/publications/sparc-reports/>, 2006.
- Timmreck, C.: Three-dimensional simulation of stratospheric background aerosol: First results of a multiannual general circulation model
- 965 simulation, *J. Geophys. Res.*, 106, 28 313–28 332, 2001.
- Toohey, M., Krüger, K., Schmidt, H., Timmreck, C., Sigl, M., Stoffel, M., and Wilson, R.: Disproportionately strong climate forcing from extratropical explosive volcanic eruptions, *Nature Geoscience*, 12, 100–107, 2019.
- Veefkind, J., Aben, I., McMullan, K., Förster, H., De Vries, J., Otter, G., Claas, J., Eskes, H., De Haan, J., Kleipool, Q., et al.: TROPOMI on the ESA Sentinel-5 Precursor: A GMES mission for global observations of the atmospheric composition for climate, air quality and
- 970 ozone layer applications, *Remote Sensing of Environment*, 120, 70–83, 2012.
- Vernier, J.-P., Thomason, L., and Kar, J.: CALIPSO detection of an Asian tropopause aerosol layer, *Geophysical Research Letters*, 38, 2011.

- von Savigny, C., Ernst, F., Rozanov, A., Hommel, R., Eichmann, K.-U., Rozanov, V., Burrows, J., and Thomason, L.: Improved stratospheric aerosol extinction profiles from SCIAMACHY: validation and sample results, *Atmospheric Measurement Techniques*, 8, 5223–5235, 2015.
- 975 von Savigny, C., Timmreck, C., Buehler, S., Burrows, J., Giorgetta, M., Hegerl, G., Horvath, A., Hoshyaripour, G. A., Hoose, C., Quaas, J., Malinina, E., Rozanov, A., Schmidt, H., Thomason, L., Toohey, M., and Vogel, B.: The Research Unit VolImpact: Revisiting the volcanic impact on atmosphere and climate ? preparations for the next big volcanic eruption, *Meteorologische Zeitschrift*, pp. –, <https://doi.org/10.1127/metz/2019/0999>, <http://dx.doi.org/10.1127/metz/2019/0999>, 2020.
- Waters, J., Froidevaux, L., Harwood, R., Jarnot, R., Pickett, H., Read, W., Siegel, P., Cofield, R., Filipiak, M., Flower, D., Holden, J., Lau, G., Livesey, N., Manney, G., Pumphrey, H., Santee, M., Wu, D., Cuddy, D., Lay, R., Loo, M., Perun, V., Schwartz, M., Stek, P., Thurstans, R., Boyles, M., Chandra, K., Chavez, M., Chen, G.-S., Chudasama, B., Dodge, R., Fuller, R., Girard, M., Jiang, J., Jiang, Y., Knosp, B., LaBelle, R., Lam, J., Lee, K., Miller, D., Oswald, J., Patel, N., Pukala, D., Quintero, O., Scaff, D., Van Snyder, W., Tope, M., Wagner, P., and Walch, M.: The Earth observing system microwave limb sounder (EOS MLS) on the aura Satellite, *IEEE Transactions on Geoscience and Remote Sensing*, 44, 1075–1092, <https://doi.org/10.1109/TGRS.2006.873771>, 2006.
- 980
- WMO: A three-dimensional science: Second session of the commission for aerology, *WMO Bull*, 4, 134–138, 1957.
- 985 WMO, W. M. O.: Polar stratospheric ozone: past, present, and future, Chapter 4 in *Scientific Assessment of Ozone Depletion: 2018*, Global Ozone Research and Monitoring Project-Report No. 58, 2018.
- Yang, K., Carn, S. A., Ge, C., Wang, J., and Dickerson, R. R.: Advancing measurements of tropospheric NO₂ from space: New algorithm and first global results from OMPS, *Geophysical Research Letters*, 41, 4777–4786, 2014.
- 990 Zhang, Y., Li, C., Krotkov, N. A., Joiner, J., Fioletov, V., and McLinden, C.: Continuation of long-term global SO₂ pollution monitoring from OMI to OMPS, *Atmospheric Measurement Techniques*, 10, 1495–1509, <https://doi.org/10.5194/amt-10-1495-2017>, <https://www.atmos-meas-tech.net/10/1495/2017/>, 2017.
- Zhu, Y., Toon, O. B., Kinnison, D., Harvey, V. L., Mills, M. J., Bardeen, C. G., Pitts, M., Bègue, N., Renard, J.-B., Berthet, G., et al.: Stratospheric aerosols, polar stratospheric clouds, and polar ozone depletion after the Mount Calbuco eruption in 2015, *Journal of Geophysical Research: Atmospheres*, 123, 12–308, 2018.
- 995